



Research Paper

Infrared study of the star-forming region associated with the UC HII regions G45.07+0.13 and G45.12+0.13

N. Azatyan , E. Nikoghosyan , H. Harutyunian, D. Baghdasaryan and D. Andreasyan

Byurakan Astrophysical Observatory, 0213, Aragatsotn Province, Byurakan, Armenia

Abstract

Ultra-compact H II (UCHII) regions are an important phase in the formation and early evolution of massive stars and a key component of the interstellar medium (ISM). The main objectives of this work are to study the young stellar population associated with the G45.07+0.13 and G45.12+0.13 UC HII regions, as well as the ISM in which they are embedded. We determined the distribution of the hydrogen column density ($N(\text{H}_2)$) and dust temperature (T_d) in the molecular cloud using Modified blackbody fitting on *Herschel* images obtained in four bands: 160, 250, 350, and 500 μm . We used near-, mid-, and far-infrared photometric data to identify and classify the young stellar objects (YSOs). Their main parameters were determined by the radiation transfer models. We also constructed a colour-magnitude diagram and K luminosity functions (KLFs) to compare the parameters of stellar objects with the results of the radiative transfer models. We found that $N(\text{H}_2)$ varies from $\sim 3.0 \times 10^{23}$ to $5.5 \times 10^{23} \text{ cm}^{-2}$ within the G45.07+0.13 and G45.12+0.13 regions, respectively. The maximum T_d value is 35 K in G45.12+0.13 and 42 K in G45.07+0.13. T_d then drops significantly from the centre to the periphery, reaching about 18–20 K at distances of ~ 2.6 and ~ 3.7 pc from InfraRed Astronomical Satellite (IRAS) 19110+1045 (G45.07+0.13) and IRAS 19111+1048 (G45.12+0.13), respectively. The gas plus dust mass value included in G45.12+0.13 is $\sim 3.4 \times 10^5 M_\odot$ and $\sim 1.7 \times 10^5 M_\odot$ in G45.07+0.13. The UCHII regions are connected through a cold ($T_d = 19$ K) bridge. The radial surface density distribution of the identified 518 YSOs exhibits dense clusters in the vicinity of both IRAS sources. The parameters of YSOs in the IRAS clusters (124 objects) and 394 non-cluster objects surrounding them show some differences. About 75% of the YSOs belonging to the IRAS clusters have an evolutionary age greater than 10^6 yr. Their slope α of the KLF agrees well with a Salpeter-type initial mass function (IMF) ($\gamma = 1.35$) for a high mass range (O–F stars, $\beta \sim 2$) at 1 Myr. The non-cluster objects are uniformly distributed in the molecular cloud, 80% of which are located to the right of the 0.1 Myr isochrone. The slope α of the KLF of non-cluster objects is 0.55 ± 0.09 , corresponding better to a Salpeter-type IMF for low-mass objects (G–M stars, $\beta \sim 1$). Our results show that two dense stellar clusters are embedded in these two physically connected UCHII regions. The clusters include several high- and intermediate-mass zero-age main sequence stellar objects. Based on the small age spread of the stellar objects, we suggest that the clusters originate from a single triggering shock. The extended emission observed in both UCHII regions is likely due to the stellar clusters.

Keywords: stars: pre-main sequence – stars: luminosity function – infrared: stars – radiative transfer – interstellar medium (ISM), nebulae

(Received 18 January 2022; revised 6 April 2022; accepted 13 April 2022)

1. Introduction

Massive stars are generally recognised to form inside dense ($n > 10^3 \text{ cm}^{-3}$) and cold ($T \sim 10\text{--}30$ K) compact clumps in giant molecular clouds (GMCs) (e.g. Lada & Lada 2003). Based on results obtained for different massive star-forming regions, star formation in these clumps appears to be triggered by compression from external shocks. Other clusters can be formed by self-gravitation of dense regions in molecular clouds (e.g. Elmegreen & Lada 1977; Zinnecker, McCaughrean, & Wilking 1993). If star formation is triggered by compression, the age spread of the new generation of stars should be small, while the age spread of young stellar clusters is expected to be larger in self-initiated condensations (Zinnecker et al. 1993).

Although few in number relative to solar-mass stars, massive stars and the star clusters hosting them are thought to play an important role in the evolution of galaxies. They affect their environment by shaping the morphology, energy, and chemistry of the interstellar medium (ISM) through phenomena such as outflows, stellar winds, and supernovae (McKee & Tan 2003). The energy injected into the surrounding neutral ISM may trigger the formation of new stars (Elmegreen & Lada 1977) or indeed the opposite effect, inhibiting star formation due to dispersal of molecular clouds (Williams & McKee 1997).

The study of massive stars involves certain difficulties (Zinnecker & Yorke 2007; McKee & Ostriker 2007). The main challenges in studying high-mass star formation include: (i) the newly formed massive stars are deeply embedded in GMCs, (ii) massive stars are rare, and (iii) they begin burning their nuclear fuel, i.e. reach the zero-age main sequence (ZAMS) while still accreting (McKee & Tan 2003; Peters et al. 2010). Understanding the formation and early evolution of massive stars requires detailed knowledge of the environments where star-forming

Corresponding author: N. Azatyan, email: nayazatyan@bao.sci.am.

Cite this article: Azatyan N, Nikoghosyan E, Harutyunian H, Baghdasaryan D and Andreasyan D. (2022) Infrared study of the star-forming region associated with the UC HII regions G45.07+0.13 and G45.12+0.13. *Publications of the Astronomical Society of Australia* 39, e024, 1–16. <https://doi.org/10.1017/pasa.2022.20>

events occur, e.g. the main properties of the surrounding material and the characteristics of the embedded stellar population.

Massive stars produce powerful Lyman continuum emission that is sufficiently energetic to ionise their surroundings and create observable ionised H II regions. These regions progress from hyper-compact through ultra-compact (UCHII) to compact and finally diffuse H II region phases, during which they either dissociate or blow out their surrounding medium (Churchwell 2002; Keto 2007). Thus, UCHII regions are thought to be the sites of the early stages of massive star formation. These represent ideal natural laboratories to investigate the influence of hot massive stars on their environment, including the morphology of their surrounding material and the triggering of star formation.

The UCHII regions are dense, compact bubbles of photoionised gas in diameter less than 0.1 pc (Wood & Churchwell 1989; Kurtz, Churchwell, & Wood 1994; Garay & Lizano 1999; Churchwell 2002), with an estimated age of 10^4 – 10^5 yr based on their spatial diameters and typical expansion rates. Most UCHII regions have been identified by their centimetre-wavelength free-free emission, as these photons can penetrate the surrounding dust cores and dense molecular gas. A study by Wood & Churchwell (1989) showed that UCHII regions are well distinguished at far- and mid-infrared wavelengths. Mid-infrared observations have also confirmed the presence of low-density extended emissions surrounding UCHII regions (e.g. de la Fuente et al. 2020a,b). The energy flux from the halo is quite large compared to that of small UCHII cores; most likely, this requires ionisation by a cluster of hot stars as the energy is usually higher than expected from single high-mass stars (Churchwell 2002).

To constrain the formation mechanisms of embedded clusters, a detailed study of the stellar and gas content in UCHII regions and their immediate neighbourhoods provides vital information. The star-forming regions associated with InfraRed Astronomical Satellite (IRAS) 19110+1045 and IRAS 19111+1048 sources, referred to as G45.07+0.13 and G45.12+0.13 UCHII regions, respectively (Wood & Churchwell 1989), are part of the Galactic Ring Survey Molecular Cloud (GRSMC) 45.46+0.05 large star formation complex (Simon et al. 2001), where several other UCHII regions are found. This complex is thus an ideal laboratory to investigate the early stages of massive star formations and their influence on natal environments.

From the images obtained at 2 and 6 cm radio wavelengths, Wood & Churchwell (1989) determined a spherical morphology of the ionised gas in the G45.07+0.13 region and a cometary shape in G45.12+0.13. In 1.3 mm continual images, G45.12+0.13 has an elliptical shape, elongated from north-east to south-west (Hernández-Hernández et al. 2014). At MIR wavelengths, both objects show extended emissions and each includes at least 2 UCHII regions (de la Fuente et al. 2020a,b). Given their proximity in the plane of the sky and similar LSR velocities, Hunter, Phillips, & Menten (1997) suggested that G45.12+0.13 and G45.07+0.13 are at the same distance (8.3 kpc). Simon et al. (2001) determined a kinematic distance of 6 kpc for the GRSMC 45.46+0.05 complex containing the two UCHII regions. Fish et al. (2003) and Han et al. (2015) obtained near and far kinematic distances for both G45.07+0.13 and G45.12+0.13 of ~ 4.0 and ~ 8.0 kpc. The estimated far distance is consistent with the previous estimate by Hunter et al. (1997) and a more recent one based on the trigonometric parallax method (7.75 ± 0.45 kpc, Wu et al. 2019). Therefore, we adopt a distance of 7.8 kpc in our study.

Multi-wavelength studies suggest that both regions are sites of active massive star formation, where IRAS 19111+1048 (G45.12+0.13) is in a more advanced stage (Hunter et al. 1997; Vig et al. 2006). Hunter et al. (1997) were the first to detect outflows from these sources. Their CO ($J = 6 - 5$) map shows bipolar outflows with an origin well centred on the radio position of both UCHII regions. The continuum-subtracted molecular hydrogen image in Persi & Tapia (2019) shows a pair of faint H₂ emission knots in G45.07+0.13. Both regions contain type-I OH masers (Argon, Reid, & Menten 2000), however, only G45.07+0.13 produces H₂O (Hofner & Churchwell 1996) and methanol maser emissions (Hernández-Hernández et al. 2019; Breen et al. 2019). The probe of massive star-forming clumps, SO $J_k = 1_0 - 0_1$ (i.e. 30 GHz) emission, has also been detected in both regions (Mateen, Hofner, & Araya 2006).

The NIR data, as well as high-resolution radio measurements, enabled Vig et al. (2006) and Rivera-Ingraham et al. (2010) to conclude that the IRAS 19111+1048 region contains numerous ZAMS stars energising a compact and evolved H II region. Liu et al. (2019) reached the same conclusion based on multi-wavelength images observed with SOFIA-FORCAST at wavelengths from ~ 10 to 40 μm . Based on integrated radio emissions, these sources' spectral types are O6-BO and the power law index of the initial mass function (IMF) is 5.3 ± 0.5 for the mass range $14 < m/M_{\text{sun}} < 33$ (Vig et al. 2006). Azatyan Nikoghosyan, & Khachatryan (2016) revealed a compact group of pre-main-sequence (PMS) objects (~ 50 members) in the vicinity of IRAS 19110+1045.

In this paper, we present the results of a near-, mid-, and far-infrared (NIR, MIR, and FIR) study of UCHII regions G45.07+0.13 and G45.12+0.13. We aim to better understand (i) the physical properties of dense molecular and ionised gas in the immediate neighbourhood of UCHII regions; (ii) the properties of embedded massive stars or star clusters; (iii) whether the formation of the embedded massive stars or star clusters was triggered; and (iv) whether the presence of a new generation of stars was triggered by the activity of the embedded star(s).

We have organised the paper as follows. Section 2 describes the used data; in Section 3.1, we discuss the properties of the gas and dust and from Sections 3.2 to 3.7, we analyse the stellar population in the region. Finally, the study results are summarised in Section 4.

2. Used data

In our study, we used data covering a wide range of NIR to FIR wavelengths. The first dataset comprises archival NIR photometric data in the J , H , and K bands of the Galactic Plane Survey DR6 (UKIDSS GPS, Lucas et al. 2008) with a resolution of $0.1'' \text{ px}^{-1}$. This survey is complete to approximately 18 mag in the K band and provides a percentage probability of an individual object being a star, galaxy, or noise.

Archival MIR observations were obtained from the Galactic Legacy Infrared Midplane Survey Extraordinaire (GLIMPSE, Churchwell et al. 2009), using the *Spitzer* Infrared Array Camera (IRAC, Fazio et al. 2004). The four IRAC bands are centred at approximately 3.6, 4.5, 5.8, and 8.0 μm with a resolution of $0.6'' \text{ px}^{-1}$. At longer wavelengths, we used data from a survey of the inner Galactic plane using the Multiband Infrared Photometer for *Spitzer* (MIPSGAL). The survey field was imaged in 24 and 70 μm

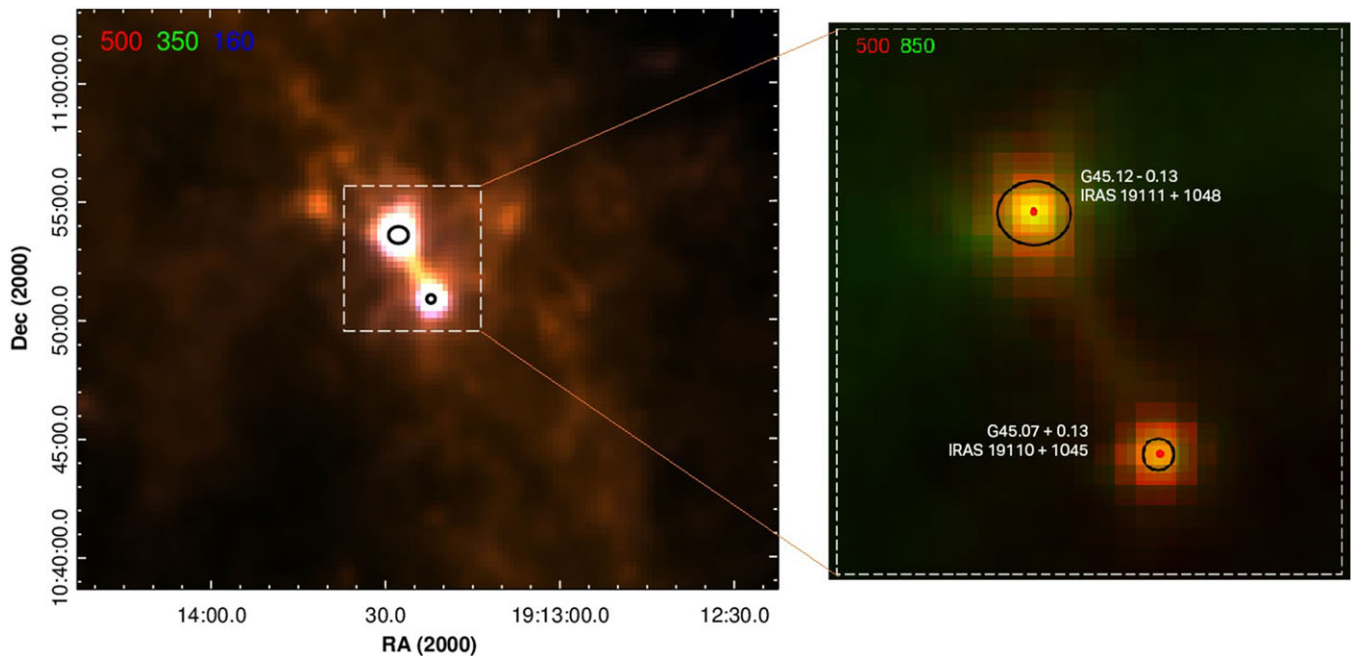


Figure 1. Colour-composite images of the G45.12+0.13 and G45.07+0.13 UC HII regions. *Left panel:* *Herschel* 160 μm (blue), 350 μm (green), and 500 μm (red); *right panel:* the zoomed area (white dotted square) at SCUBA 850 μm (green) and *Herschel* 500 μm (red). The positions and dimensions of the radio sources obtained at 2- and 6-cm wavelengths in Wood & Churchwell (1989) are marked by black circles. A red dot represents the position of an IRAS source.

passbands with resolutions of $6'' \text{ px}^{-1}$ and $18'' \text{ px}^{-1}$, respectively (Carey et al. 2009); however, only 24 μm data were available for the studied star-forming region. The point source photometric data in this star-forming region were downloaded from the NASA/IPAC Infrared Science Archive. We also used Wide-field Infrared Survey Explorer (WISE, Wright et al. 2010) data in the 3.4, 4.6, 12, and 22 μm bandpasses and Midcourse Space Experiment (MSX, Price et al. 2001) full-plane survey data in the 8.28, 12.13, 14.65, and 21.3 μm bands, which are accessible through Vizier.

To study gas and dust, as well as deeply embedded point sources, we used FIR observations, in the 70–500 μm range, obtained with the Photodetector Array Camera and Spectrometer (PACS, Poglitsch et al. 2010) and the Spectral and Photometric Imaging Receiver (SPIRE, Griffin et al. 2010) on board the 3.5 m *Herschel* Space Observatory (Pilbratt et al. 2010). For our analyses, we used photometric data and images from the PACS 70 and 160 μm catalogues, in addition to *Herschel* infrared Galactic Plane Survey (Hi-GAL, Molinari et al. 2016) data at 70, 160, 250, 350, and 500 μm . The corresponding *Herschel* half-power beamwidth (HPBW) values are $5.0''$ at 70 μm , $11.4''$ at 160 μm , $17.8''$ at 250 μm , $25.0''$ at 350 μm , and $35.7''$ at 500 μm . The point and extended source photometry were downloaded from the NASA/IPAC Infrared Science Archive. For objects with measured fluxes in both the PACS and Hi-GAL catalogues, we selected the Hi-GAL photometric data.

3. Results and discussion

3.1. Dust emission

The Hi-GAL observations provide a complete and unbiased view of continuum emission in the Galactic plane in 70, 160, 250, 350, and 500 μm bands. This wavelength range covers the peak of the

spectral energy distribution of cold dust emission, constraining important ISM parameters such as the hydrogen column density ($N(\text{H}_2)$) and the dust temperature (T_d).

In Figure 1, we present a colour-composite image (left panel) of three Hi-GAL bands (PACS 160 μm and SPIRE 350 and 500 μm) covering the molecular cloud. The G45.12+0.13 and G45.07+0.13 UC HII regions stand out sharply in terms of brightness. The black circles coincide with the positions and dimensions of radio continuum radiation (Wood & Churchwell 1989). These sources align well with the brightest part of the 850 μm emission (right panel). Figure 1 shows that both UC HII regions are embedded in a molecular cloud, with clear clump-like and filamentary structures. The images also indicate that the UC HII regions are connected by a relatively colder bridge and are thus very likely a physically bound system.

Figure 2 shows a colour-composite image of *Spitzer* IRAC 3.6 and 8.0 μm , and SPIRE 500 μm bands, illustrating that the UC HII regions are also very bright in the MIR wavelength range. This indicates a relatively high ISM temperature in the vicinity of the UC HII regions and, therefore, the presence of a significant number of hot stars (Vig et al. 2006; Rivera-Ingraham et al. 2010). This is also confirmed by the stellar population study results in this work (see the text below). Furthermore, the MIR image is saturated in the centre of both regions, which is the case for several UC HII regions (Churchwell 2002; de la Fuente et al. 2020a). In Figure 2, the arrow shows a small clumpy structure coinciding with the MSX G045.1663+00.0910 object. Three objects from the Bolocam Galactic Plane Survey (BGPS) are located within the external *Herschel* 500 μm contour; of these objects 6535 and 6536 in the Bolocat V2.1 catalogue (Ellsworth-Bowers et al. 2015) are associated with IRAS 19110+1045 and IRAS 19111+1048, respectively. The third object (6737) is associated with MSX G045.1663+00.0910. The distance estimates for these three BGPS objects are almost identical (7.5–7.9 kpc,

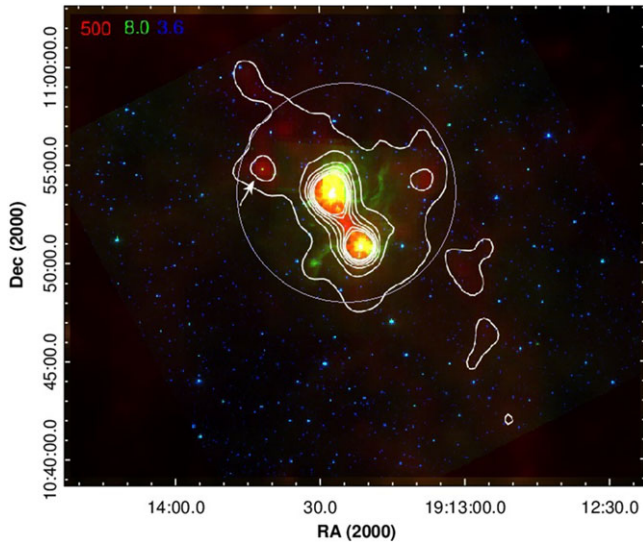


Figure 2. Colour-composite image of the G45.12+0.13 and G45.07+0.13 UC HII regions: *Spitzer* IRAC 3.6 μm (blue), 8.0 μm (green) and *Herschel* 500 μm (red). The latter is also shown with a white isophotes. The external isophot corresponds to a surface brightness of 0.55 Jy pix^{-1} , which exceeds the background $\sigma = 0.18 \text{ Jy pix}^{-1}$ by three-fold. Difference between the isophotes level is 0.25 Jy pix^{-1} . The white arrow shows a small clumpy structure around the MSX G045.1663+00.0910 object. The circle outlines an area with a radius of 6 arcmin, which almost completely covers the region of study.

Ellsworth-Bowers et al. 2015), consistent with the findings of Wu et al. (2019) and confirming that they belong to the same star formation region. We also would like to highlight the filamentary structure directed north-east towards the most extended part of the GRSMC 45.46+0.05 molecular cloud, to which UC HIIIs G45.12+0.13 and G45.07+0.13 belong (Simon et al. 2001).

Dust emission in the FIR range can be modelled as a modified blackbody $I_\nu = k_\nu \mu_{\text{H}_2} m_{\text{H}} N(\text{H}_2) B_\nu(T_d)$, where k_ν is the dust opacity, $\mu_{\text{H}_2} = 2.8$ representing the mean weight per hydrogen molecule (Kauffmann et al. 2008), m_{H} is the mass of hydrogen, $N(\text{H}_2)$ is the hydrogen column density, and $B_\nu(T_d)$ is the Planck function at dust temperature T_d .

The dust opacity in the FIR is usually parameterised as a power law normalised to the value k_0 at a reference frequency ν_0 such that $k_\nu = k_0 (\nu/\nu_0)^\beta \text{ cm}^{-2} \text{ g}^{-1}$. Following Hildebrand (1983), Könyves et al. (2015), we adopted $k_0 = 0.1 \text{ cm}^{-2} \text{ g}^{-1}$ at 300 μm (i.e. gas-to-dust ratio of 100) and $\beta = 2$. Roy et al. (2014) showed that this assumption is valid within better than 50% of the bulk of molecular clouds. We used four intensity maps from 160 to 500 μm to derive $N(\text{H}_2)$ and T_d maps. Based on the discussion in previous studies (e.g. Battersby et al. 2011), we excluded the 70 μm data as the optically thin assumption may not hold. In addition, the emission here would have a significant contribution from a warm dust component, thus, modelling with a single-temperature blackbody would over-estimate the derived temperature. The three shortward intensity maps were degraded to the spatial resolution of the 500 μm band; the four maps were then translated to a common coordinate system using $14''$ pixels at all wavelengths.

The SED fitting procedure was executed pixel by pixel. Following Pezzuto et al. (2021), we created a grid of models by varying only the temperature in the range $5 \leq T_d(\text{K}) \leq 50$ in steps of 0.01 K; for each temperature T_j , the code computes the intensity at FIR wavelengths for all bands. Since I_ν is linear with $N(\text{H}_2)$, we

can compute the column density for each pixel using the least-squares technique. The uncertainty values of I_ν for SPIRE and PACS are 10% and 20%, respectively (Könyves et al. 2015).

From the derived column density values, we estimate the mass of the dust clumps using the following expression:

$$M_{\text{clump}} = \mu_{\text{H}_2} m_{\text{H}} \text{Area}_{\text{pix}} \sum N(\text{H}_2), \quad (1)$$

where Area_{pix} is the area of a pixel in cm^2 , i.e. we calculated the mass in each pixel and then summed over all pixels within the radius.

The $N(\text{H}_2)$ and T_d maps of the wider region surrounding the G45.12+0.13 and G45.07+0.13 UC HII objects are shown in Figure 3. Both UC HII regions are distinct from the molecular cloud due to their high dust temperature and column density with an almost spherically symmetric distribution. In general, within both regions, T_d varies from about 17 to 40 K and $N(\text{H}_2)$ varies from about $3.0 \times 10^{23} \text{ cm}^{-2}$ to $5.5 \times 10^{23} \text{ cm}^{-2}$, consistent with other UC HIIIs (Churchwell, Sievers, & Thum 2010).

G45.07+0.13. In this region, the IRAS source is somewhat offset from the density maximum, which is $\sim 5.0 \times 10^{23} \text{ cm}^{-2}$. Near IRAS 19110+1045, the column density is $\sim 3.5 \times 10^{23} \text{ cm}^{-2}$. This value agrees well with the data obtained in Churchwell et al. (2010) (i.e. $3.0 \times 10^{23} \text{ cm}^{-2}$) and is almost an order of magnitude smaller than the value of Hernández-Hernández et al. (2014) ($2.7 \times 10^{24} \text{ cm}^{-2}$). In both studies, the results were obtained based on millimetre observations. The IRAS source is located close to the dust temperature maximum ($T_d = 42 \text{ K}$). This value is consistent with the data obtained in the submillimetre range ($T = 42.5 \text{ K}$, Rivera-Ingraham et al. 2010), and, within error, with the data presented in Hernández-Hernández et al. (2014) ($T = 82_{-39}^{+25} \text{ K}$). As shown in Figure 3, the dust temperature drops significantly from the centre to the periphery, reaching a value of about 18–20 K. Beyond around a 5-pixel ($\sim 1.2'$ or $\sim 2.6 \text{ pc}$) distance from the IRAS source, T_d remains constant. This may correspond to the extent of the region of influence of the ionising source(s). The size of this region correlates with the size of the extended emission ($1' \times 1'$, de la Fuente et al. 2020a), and this region's mass is $\sim 1.7 \times 10^5 M_\odot$.

G45.12+0.13. In this region, the position of IRAS 19111+1048 coincides with the maxima of both the column density ($5.5 \times 10^{23} \text{ cm}^{-2}$) and temperature (35 K). Our $N(\text{H}_2)$ value exceeds that presented in Churchwell et al. (2010) by more than an order of magnitude, however, it is comparable with the value obtained through analysis of the multi-transition ^{13}CO emission (Churchwell, Walmsley, & Wood 1992). The T_d value is in good agreement with the data presented in Rivera-Ingraham et al. (2010) ($T = 39 \text{ K}$). The isotherms are slightly elongated towards the northwest (Figure 3), which may relate to the presence of two UC HIIIs (G45.12+0.13 and G45.13+0.14) that are separated from each other in a northwest direction (de la Fuente et al. 2020a). Similar to G45.07+0.13, the dust temperature in G45.12+0.13 drops significantly further from the centre, reaching a value of around 18–20 K in its periphery. The T_d decline levels out at around 7 pixels ($\sim 1.6'$ or $\sim 3.7 \text{ pc}$) from the IRAS source. As above, the size of this region correlates with the size of the extended emission ($1.5' \times 1.5'$, de la Fuente et al. 2020a). The larger radius of the ionised region indicates that the physical extent of ionised gas around IRAS 19111+1048 is larger than that of its neighbour IRAS 19110+1045 (Vig et al. 2006). The mass of this region is $\sim 3.4 \times 10^5 M_\odot$.

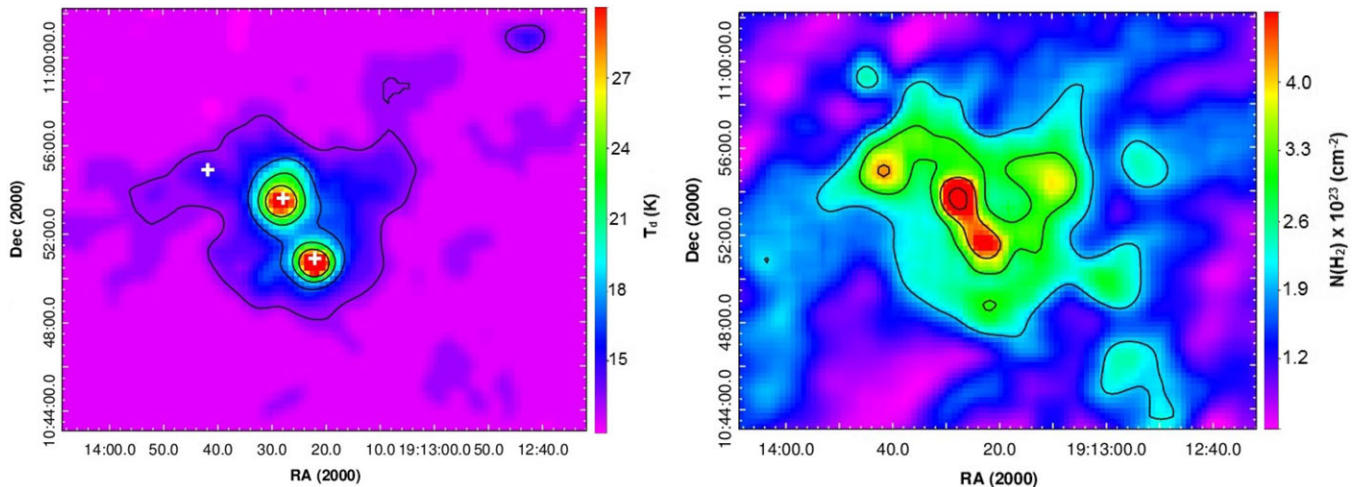


Figure 3. Maps of the $N(\text{H}_2)$ (left panel) and T_d (right panel) of the region. On the T_d map, the outer isotherm corresponds to 13 K and the interval between isotherms is 4 K. On the $N(\text{H}_2)$ map, the outer isodense corresponds to $2.0 \times 10^{23} \text{ cm}^{-2}$ and interval between isodenses is $1.0 \times 10^{23} \text{ cm}^{-2}$. The positions of the IRAS and BGPC 6737 sources are marked by white crosses.

In both regions, the extent of the ionised area significantly exceeds the size of the UCHII radio cores. Previous studies have shown that many UCHII regions are surrounded by extended emission (on an arc-minute scale) produced by low-density ionised halos (Churchwell 2002; de la Fuente et al. 2020a,b, and ref. therein). The energy flux from these halos is quite large relative to that of the small UCHII cores, implying ionisation by a cluster of hot stars rather than a single star (Churchwell 2002).

In Figure 3, a region with relatively high density ($N(\text{H}_2) \approx 4.3 \times 10^{23} \text{ cm}^{-2}$) and low temperature ($T_d \approx 19 \text{ K}$) is positioned between the two UCHII regions. This region coincides with the bridge between the UCHII regions, which is also distinguishable in the *Herschel* and *Spitzer* images (Figures 1 and 2), as well as on the $\text{H}30\alpha$ maps (Churchwell et al. 2010), suggesting that these UCHII regions are physically connected.

The distribution of the hydrogen column density in the surrounding molecular cloud has a complex, clumpy structure—in general, outwards from the UCHII regions, $N(\text{H}_2)$ varies from about 3.0 to $0.5 \times 10^{23} \text{ cm}^{-2}$ and T_d varies from about 16 to 12 K. Figure 3 shows that the ISM forms a well-defined concentration around the BGPS 6737 object; here, the column density value increases to $\sim 4.3 \times 10^{23} \text{ cm}^{-2}$.

3.2. Stellar population

3.2.1. Selection of stellar objects

To select and study the potential stellar members of the star-forming region, we focused on the part of the molecular cloud where the surface brightness at $500 \mu\text{m}$ exceeds the background by 3σ . This forms a circle with a 6 arcmin radius around the geometric centre $\alpha = 19:13:24.2$, $\delta = +10:53:38$, as shown in Figure 2. The identification of stellar objects was performed with GPS UKIDSS-DR6 as the main catalogue, and then other MIR and FIR catalogues were cross-matched with it.

The GPS UKIDSS-DR6 catalogue provides the probability of an object being a star, galaxy, or noise based on its image profile. The UKIDSS team recommends that sources classified as noise should be excluded since most of them are not real sources (Lucas et al. 2008). However, ‘galaxies’ and ‘probable galaxies’ should be

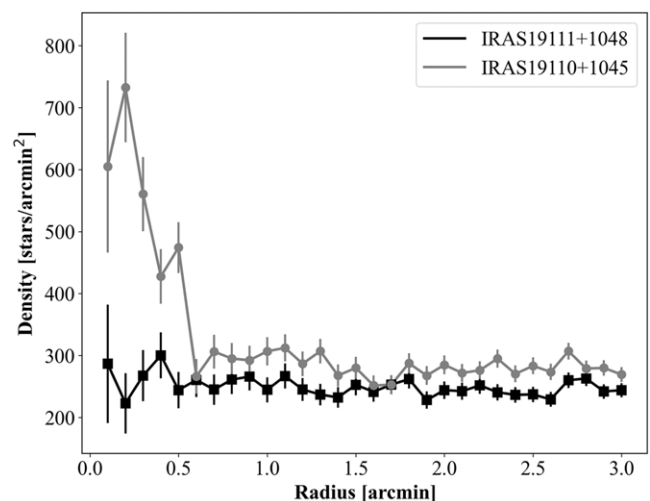


Figure 4. Radial distribution of the stellar densities relative to IRAS 19111+1048 (black line) and IRAS 19110+1045 (grey line) sources, respectively. Vertical lines are standard errors.

included in the full search, since many of these are unresolved pairs of stars or nebulous stars and could be potential members of the star-forming region. Therefore, we selected objects with a $<30\%$ probability of being noise and a magnitude of $K < 18.02$ mag, taking into account the K band limit of the UKIDSS survey. In addition, we removed objects with zero errors of measured magnitudes in the J , H , and K bands. This yielded a total of approximately 28 000 objects.

To confirm the existence of clusters in the vicinity of both IRAS sources, we constructed the radial density distribution of stars with respect to IRAS 19110+1045 and IRAS 19111+1048 (grey line and black line, respectively, Figure 4). The stellar density was determined in rings of width $0.1'$ by dividing the number of stars by the surface area. The standard error for the number of stars in each ring is used as a measure of uncertainty. The radial density distribution of the stars shows a well-defined concentration of stars around the IRAS 19110+1045 source, confirming

Table 1. Properties of the catalogues cross-matched with the GPS UKIDSS-DR6.

Catalogue name	Positional accuracy (arcsec)	3σ of combined error (arcsec)	Reference
(1)	(2)	(3)	(4)
GPS UKIDSS-DR6	0.3	—	1
GLIMPSE	0.3	1.2	2
ALLWISE	1	3	3
MIPSGAL	1	3	4
MSX	3.3	10	5
IRAS	16	48	6
PACS: Extended source	2.4	7.2	7
PACS: 70 μm	1.5	5	8
PACS: 160 μm	1.7	5.2	9
Hi-GAL: 70, 160, 250, 350, 500 μm	2	6.1	10

1. Lucas et al. (2008); 2. Churchwell et al. (2009); 3. Wright et al. (2010); 4. Carey et al. (2009); 5. Egan et al. (2003); 6. Neugebauer et al. (1984); 7. Maddox et al. (2017); 8. Poglitsch et al. (2010); 9. Poglitsch et al. (2010); 10. Sánchez-Portal et al. (2014).

Notes. (1) Name of used catalogue, (2) Positional accuracy of each catalogue, (3) 3σ of combined error of the cross-matched catalogues, (4) Source of used data.

the existence of a cluster. Starting from a $\sim 0.8'$ radius, the stellar density does not exceed the average density of the field. The existence of a cluster around the IRAS 19111+1048 source is not well-defined and no density concentration was recorded around the MSX G045.1663+00.0910 source.

The MIR and FIR photometric catalogues were cross-matched with the GPS UKIDSS-DR6 catalogue within 3σ of the combined error-matching radius (Col. 3 in Table 1). Matching radii were evaluated considering the positional accuracy of each catalogue (Col. 2 in Table 1). Sometimes, the matching radii were quite large, especially for the FIR catalogues. Additionally, multiple NIR objects can be identified by only one FIR object; in such cases, priority was given to the object with significantly higher brightness in the NIR/MIR range. If necessary, we selected the closest one by coordinates. When it was not possible to identify a single object, we did not use those FIR data to avoid possible errors. The set of steps that we used to identify young stellar objects (YSOs) in the combined photometric catalogue is presented in the following sub-sections.

3.2.2. Colour-colour diagrams

When selecting potential members of the cluster from stars located in the direction of the molecular cloud, we assumed that most of the members of the considered active star-forming region are YSOs. One of the main observational characteristics of YSOs is an IR excess due to the presence of circumstellar discs and envelopes (Lada & Lada 2003; Hartmann 2009); furthermore, the measure of the IR excess in the NIR and/or MIR ranges can be used to characterise the evolutionary stage of a YSO (Class I and Class II). Therefore, YSO candidates can be identified based on their position in colour-colour (*c-c*) diagrams. The choice of colours depends on the available data. We constructed six (*c-c*) diagrams, as shown in Figure 5. The same approach has previously been successfully applied to the IRAS 05168+3634 star-forming region (Azatyan 2019).

Objects with IR excess were first identified using the (*J-H*) versus (*H-K*) *c-c* diagram shown in Figure 5 (top left panel). The

solid and dashed curves represent the loci of the intrinsic colours of dwarf and giant stars (Bessell & Brett 1988) converted to the CIT system (Carpenter 2001); the parallel solid lines drawn from the base and tip of these loci are the interstellar reddening vectors (Rieke & Lebofsky 1985). The locus of unreddened classical T Tauri stars (CTTSs) is taken from Meyer et al. (1997). The region where the intermediate-mass PMS stars, i.e. Herbig Ae/Be stars, are usually found is bounded by dashed lines (Hernández et al. 2005). Objects with different evolutionary stages occupy specific areas of this diagram (Lada & Adams 1992): (i) Classical Be stars, (ii) objects located to the left, and (iii) objects located to the right of reddening vectors. Classical Be stars have $J-K < 0.6$ and $H-K < 0.3$ colour indices, which we removed from the final list.

The deviation of YSOs from the main sequence (MS) on this diagram can have two causes: the presence of IR excess and interstellar absorption, which also leads to objects reddening. In the latter case, deviation from the MS will be directed along the reddening vectors. The IR excess of objects located to the right of reddening vectors cannot be caused solely by interstellar absorption and, at least partially, their IR excess is caused by the existence of a circumstellar disc and envelope. Therefore, objects located to the right of the reddening vectors can be considered YSO candidates. Among the objects located in the reddening band of MS and giants, we classified those that have a (*J-K*) > 3 mag colour index as Class I evolutionary stage YSOs (Lada & Adams 1992). These are located in the upper right corner of the diagram. A total of 5,135 YSO candidates were selected using the (*J-H*) versus (*H-K*) *c-c* diagram.

Other objects in the reddening band are generally considered to be either field stars or Class III objects with small NIR excess. The latter objects can be potential members of the star-forming region, however, differentiating between field stars and Class III objects is very difficult. Thus, we added to the final list those objects from this sample that were classified as Class I and Class II evolutionary stage YSOs in at least two other *c-c* diagrams.

Not all objects in the main sample were detected in the *J*, *H*, and *K* bands simultaneously. Accordingly, we used data from the GLIMPSE catalogue to combine NIR and MIR photometry to identify sources with IR excesses and compile a more complete excess/disc census for the region. Since the 4.5 μm band is the most sensitive of the four IRAC bands to YSOs (Gutermuth et al. 2008), we used a *K*-[3.6] versus [3.6]-[4.5] *c-c* diagram. The [3.6]-[4.5] colour is dominated by accretion rate, with higher accretion rate sources appearing redder (Allen et al. 2004). Figure 5 (top right panel) shows the *K*-[3.6] versus [3.6]-[4.5] *c-c* diagram, with diagonal lines outlining the YSO location region and a dashed line separating the Class I and Class II object domains. The arrow shows the extinction vector (Flaherty et al. 2007). All lines are taken from Allen et al. (2007). A total of 1 016 YSO candidates were selected using the *K*-[3.6] versus [3.6]-[4.5] *c-c* diagram.

The MIR SEDs of Class I and Class II objects are dominated by emission from dusty circumstellar material, allowing them to be readily distinguished from pure photospheric sources such as unrelated field stars and indistinguishable diskless members. *Spitzer* is advantageous for studying such regions since its imaging instruments (IRAC at 3.6–8 μm and MIPS at 24–160 μm) are targeted at the MIR wavelengths, which are less affected by extinction from dust in comparison to NIR (Gutermuth et al. 2008). Since the IRAC 8 μm band overlaps with silicate features, reddened photospheres would appear increasingly blue in [5.8]-[8.0] colour (Megeath et al. 2004). Figure 5 (middle left and right panels) shows

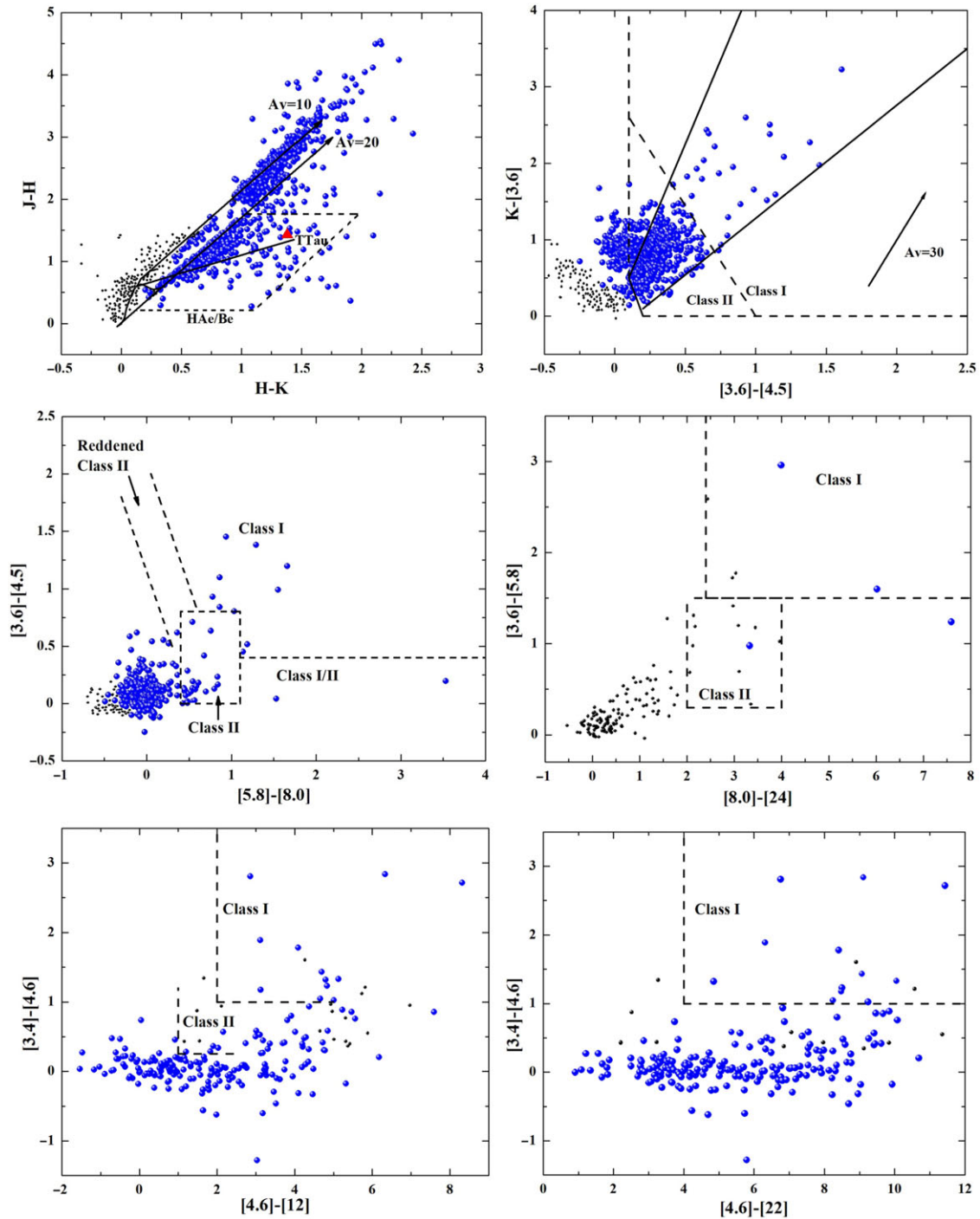


Figure 5. Colour-colour diagrams of the region. *Top left panel:* $(J-H)$ versus $(H-K)$ diagram. The dwarf and giant loci (solid and dashed curves, respectively) are from Bessell & Brett (1988) and were converted to the CIT system (Carpenter 2001). The parallel lines represent the interstellar reddening vectors (Rieke & Lebofsky 1985). The locus of unreddened classical T Tauri stars is from Meyer et al. (1997). The region bounded by dashed lines is the Herbig Ae/Be stars location (Hernández et al. 2005). *Top right panel:* $K-[3.6]$ versus $[3.6]-[4.5]$ diagram. In this diagram, Classes I and II domains are separated by the dashed line. The arrow shows the extinction vector (Flaherty et al. 2007). All the lines are from Allen et al. (2007). *Middle left panel:* $[3.6]-[4.5]$ versus $[5.8]-[8.0]$ diagram. Two parallel dashed lines border the positions of reddened Class II objects. The horizontal dashed line shows the adopted division between Class I and Class I/II sources. The dashed rectangle shows the position of Class II sources. All the lines are from Megeath et al. (2004). *Middle right panel:* $[3.6]-[5.8]$ versus $[8.0]-[24]$ diagram. The horizontal and vertical dashed lines separate Class I sources in this region. The dashed rectangle shows the position of Class II sources. All the lines are from Muzerolle et al. (2004). *Bottom left and right panels:* $[3.4]-[4.6]$ versus $[4.6]-[12]$ and $[3.4]-[4.6]$ versus $[4.6]-[22]$ diagrams. The blue circles are selected YSO candidates and black circles are non-classified ones. Not all non-classified objects are presented in these diagrams. IRAS 19111+1048 source is indicated by a red triangle.

c-c diagrams with different combinations of *Spitzer* wavelengths distinguishing YSOs from both Class I and Class II evolutionary stages. In the middle-left panel, we used *Spitzer* IRAC wavelengths. Objects located around the $([3.6]-[4.5]; [5.8]-[8.0])=(0;0)$ region are stars with the colours of the stellar photosphere and diskless PMS (i.e. Class III) objects. Class II objects fall within the $0 < [3.6]-[4.5] < 0.8$ and $0.4 < [5.8]-[8.0] < 1.1$ range. Objects with $[3.6]-[4.5] > 0.8$ and $[5.8]-[8.0] > 1.1$ range likely correspond to a Class I evolutionary stage (Allen et al. 2004; Megeath et al. 2004; Qiu et al. 2008). Three sources exhibit colours inconsistent with Class I, Class II, or reddened photosphere models. One source exhibits a higher $[3.6]-[4.5]$ colour value than Class II objects, but lower $[5.8]-[8.0]$ colour than Class I objects. We identify this source as a reddened Class II object. The other two sources have $[5.8]-[8.0] > 1.1$, consistent with Class I objects, but $[3.6]-[4.5] < 0.4$, which is lower than predicted by Class I models (Allen et al. 2004). Since these objects share the properties of Class I and Class II sources, we refer to them as Class I/II (Megeath et al. 2004). In total, 42 YSO candidates were selected using the $[3.6]-[4.5]$ versus $[5.8]-[8.0]$ c-c diagram.

The $24\ \mu\text{m}$ channel is the primary means of identifying optically thin dust discs. Since photospheric colours should be close to zero for all spectral types, the $[8.0]-[24]$ colour is particularly sensitive to excess (Muzerolle et al. 2004). In the middle right panel of Figure 5, we used *Spitzer* IRAC and MIPS wavelengths to plot a $[3.6]-[5.8]$ versus $[8.0]-[24]$ c-c diagram. Sources clustered around $[3.6]-[5.8] \approx 0$ and $0 \leq [8.0]-[24] \leq 1$ probably represent a mixture of pure photospheres and perhaps some modest $24\ \mu\text{m}$ excess. Class I and Class II evolutionary stage YSOs have strong $[8.0]-[24]$ excesses and moderate-to-strong $[3.6]-[5.8]$ excesses. Therefore, objects with $[3.6]-[5.8] > 1.5$ and $[8.0]-[24] > 2.4$ colours are likely to be Class I sources with envelopes. Class II objects with optically thick discs exhibit $[3.6]-[5.8] > 0.3$ and $[8.0]-[24] > 2$ colour values (Muzerolle et al. 2004; Caulet, Gruendl, & Chu 2008). Using the $[3.6]-[5.8]$ versus $[8.0]-[24]$ c-c diagram, we selected 17 YSO candidates.

Additionally, we constructed two other MIR c-c diagrams using the list of objects with good WISE detections, i.e. those possessing photometric uncertainty < 0.2 mag in WISE bands. The lower left panel shows the $[3.4]-[4.6]$ versus $[4.6]-[12]$ c-c diagram. Similar to the previous cases, objects with different evolutionary stages fall within certain areas of this diagram (Koenig et al. 2012). Class I YSOs are the reddest objects, with $[3.4]-[4.6] > 1.0$ and $[4.6]-[12] > 2.0$. Class II YSOs are slightly less red objects and have $[3.4]-[4.6]-\sigma([3.4]-[4.6]) > 0.25$ and $[4.6]-[12]-\sigma([4.6]-[12]) > 1.0$, where $\sigma(\dots)$ indicates the combined photometric error, added in quadrature. A total of 130 YSO candidates were selected using the $[3.4]-[4.6]$ versus $[4.6]-[12]$ c-c diagram.

The accuracy of the previous classification of stars with photometric errors < 0.2 mag can be verified using WISE band 4. Previously classified Class I sources were re-classified as Class II if $[4.6]-[22] < 4.0$, and the Class II stars were returned to the unclassified pool if $[3.4]-[12] < -1.7 \times (([12]-[22]) + 4.3)$ (Koenig et al. 2012). There were no incorrect selections in the pre-classified objects in bands 1–3, confirming the results obtained in the $[3.4]-[4.6]$ versus $[4.6]-[12]$ c-c diagram (Figure 5, lower right panel).

3.2.3. α_{IRAC} slope

Examining the IR SEDs of YSOs is one of the most robust methods for identifying the presence of a circumstellar disc. The shape of

the SED can distinguish a disc origin for the observed IR excesses from other possible causes. A particularly useful measure of the shape of a SED is its slope, which is defined as $\lambda F_\lambda \propto \lambda^{\alpha_{IRAC}}$ (Lada 1987). We measured the α_{IRAC} slope values for each of the sources detected in all four IRAC bands (3–8 μm). Diskless stars (i.e. stellar photospheres) are characterised by $\alpha_{IRAC} < -2.56$ (Class III), while evolved discs fall within the $-2.56 < \alpha_{IRAC} < -1.8$ range (Class II/III). Class II evolutionary stage objects have values in the $-1.8 < \alpha_{IRAC} < 0$ range, while Class I evolutionary stage objects are characterised by $\alpha_{IRAC} > 0$ (Hartmann et al. 2005; Lada et al. 2006). The selection of YSOs by α_{IRAC} slope is based on the same fluxes as used in the $[3.6]-[4.5]$ versus $[5.8]-[8.0]$ c-c diagram, however, in this case, 186 objects were added to the YSO candidates.

3.2.4. Extraction of field contamination

While IR excess is a powerful membership diagnostic tool for young and embedded sources, many potential contaminants exhibit IR excess. There are two main classes of extragalactic contaminants that can be misidentified as YSOs (Stern et al. 2005). One is star-forming galaxies and narrow-line active galactic nuclei (AGNs), which have growing excesses at 5.8 and 8.0 μm due to hydrocarbon emission. The other is broad-line AGNs, which have IRAC colours very similar to those of YSOs. Gutermuth et al. (2008) developed a method based on the Bootes Shallow Survey data to substantially mitigate these contaminants. In this method, hydrocarbon emission sources, including galaxies and narrow-line AGNs, can be eliminated based on their positions in the $[3.6]-[5.8]$ versus $[4.5]-[8.0]$ diagram. The broad-line AGNs, which are typically fainter than YSOs in the *Spitzer* bands, are identified by their positions in the $[4.5]$ versus $[4.5]-[8.0]$ colour-magnitude diagram.

We firstly checked our list of YSOs according to the conclusions of Stern et al. (2005), i.e. galaxies dominated by PAH emission should have MIR colours that occupy a relatively unique area of most IRAC c-c diagrams: $[3.6]-[5.8] < 1.5 \times (([4.5]-[8.0]-1)/2)$, $[3.6]-[5.8] < 1.5$, and $[4.5]-[8.0] > 1$. Notably, no sources on our list satisfied these conditions. By initially filtering out PAH sources, we can construct a filter that more closely traces the broad-line AGN distribution and then use the $[4.5]$ versus $[4.5]-[8.0]$ colour-magnitude diagram to flag likely broad-line AGNs according to the conditions of Gutermuth et al. (2008) and Qiu et al. (2008): $[4.5]-[8.0] > 0.5$, $[4.5] > 13.5 + (([4.5]-[8.0]-2.3)/0.4)$, and $[4.5] > 13.5$. In total, 26 sources satisfied these conditions on our list, 14 of which were already classified as YSOs from other c-c diagrams. Among our selected YSOs, we also applied a condition (i.e. $[4.5] > 7.8$ mag and $[8.0]-[24.0] < 2.5$ mag) to identify possible AGB contaminants (Robitaille et al. 2008). In total, 113 sources were identified as possible AGB stars among our list, 64 of which were already classified as YSOs in other c-c diagrams. Thus, in total, we removed 78 objects from the list of YSO candidates.

3.2.5. YSO candidates

The investigated region is quite distant and large, thus, there is a high probability of selecting objects that do not belong to the molecular cloud. On the other hand, PMS objects with comparatively small NIR excesses may be located in the reddening band and are therefore excluded from the selection. To minimise the likelihood of making an incorrect selection, we selected YSOs on the criterion of being stars classified as objects with IR excess by at least two different selection methods, i.e. the c-c diagrams and

α_{IRAC} slope. However, since the region has two saturated areas in the MIR band around the IRAS objects (IRAS 19110+1045 with 25'' radius and IRAS 19111+1048 with 50'' radius), this can lead to the potential loss of objects belonging to the molecular cloud. Accordingly, objects within those areas classified as YSOs based on only the NIR *c-c* diagram were included in the list of candidate YSOs. We selected the dominant evolutionary stage for each object in our chosen methods. In the case of equality, the older stage was selected. In the *c-c* diagrams, Class I and Class II YSOs are indicated with blue filled circles. Non-classified objects are shown with black circles.

In total, we selected 909 YSOs within a 6 arcmin radius, which include 849 Class II and 60 Class I objects. Among these, 56 objects were selected based on MIR photometric data.

3.3. SED analysis

To confirm the selected YSOs and to determine their parameters, we constructed their SEDs and fitted them with the radiative transfer models of Robitaille et al. (2007). These models assume an accretion scenario in the star formation process, where a central star is surrounded by an accretion disc, an infalling flattened envelope, and the presence of bipolar cavities. We used the command-line version of the SED fitting tool where numerous precomputed models are available. This procedure was performed using wavelengths ranging from 1.1 to 500 μm , in particular, *J*, *H*, and *K* (UKIDSS); 3.6, 4.5, 5.8, and 8.0 μm (*Spitzer* IRAC); 24 μm (*Spitzer* MIPS); 3.4, 4.6, 12, and 22 μm (WISE); 70 and 160 μm (*Herschel* PACS); and 70, 160, 250, 350, and 500 μm (Hi-GAL). We considered as an upper limit the FIR fluxes that were identified as closest by coordinates to the NIR object to avoid possible errors (see Section 3.2.1). For the interstellar extinction, we chose an interval of 10–100 mag that would exceed the results obtained by COBE/DIRBE and IRAS/ISSA maps ($A_V = 10\text{--}50$ mag, Schlegel, Finkbeiner, & Davis 1998). The distance interval corresponds to the estimates made in the previous studies (6.5–9.5 kpc, see Introduction).

To identify the representative values of different physical parameters, the tool retrieved the best-fit model and all models that exhibited differences between χ^2 values and the best χ^2 smaller than $3N$, where N is the number of data points used (Robitaille et al. 2007). This approach was chosen because the sampling of the model grid is too sparse to effectively determine the minima of the χ^2 surface and consequently obtain the confidence intervals.

As we selected YSOs in two MIR-saturated regions using only their *J*, *H*, and *K* magnitudes (see Section 3.2.5), constructing their SEDs based on only three photometric data points does not provide a reliable basis for any conclusions (115 YSOs). Excluding these objects, we achieved relatively robust parameters for 431 of the 793 selected YSOs (16 Class I and 415 Class II) with $\chi^2 < 100$ that composes 55% of the total number. The fact that reliable parameters could not be determined for the remaining 45% of objects can be explained by several reasons, which likely include errors in the identification and selection of objects.

To estimate the reliability of the results obtained by the SED fitting tool, we carried out the same analysis in a control field. For Control field 1, we selected a region located in the vicinity of but outside the GRSMC 45.46+0.05 star-forming region (Simon et al. 2001). Figure 6 shows the position of Control field 1 with the same 6 arcmin radius. The stellar population analysis of the Control

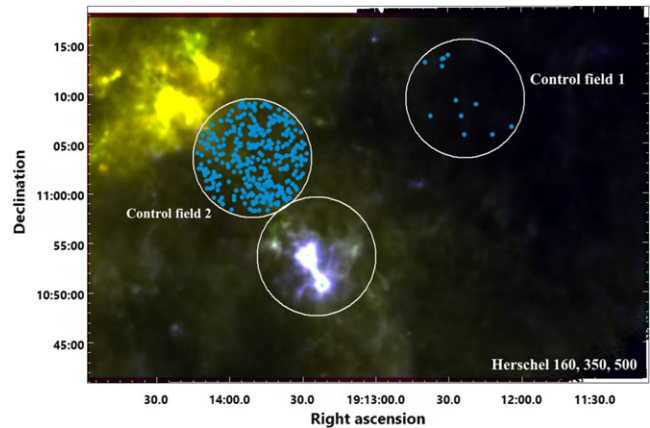


Figure 6. *Herschel* 160 (blue), 350 (green), 500 (red) μm colour-composite image of the considered region and two Control fields with the same 6 arcmin radius around the centres with coordinates α (2000) = 19:12:22.86, δ (2000) = 11:09:30.7 (Control field 1), and α (2000) = 19:13:52.96, δ (2000) = 11:03:23.5 (Control field 2). YSOs selected by SED fitting tool (see Section 3.3) in both Control fields are indicated in filled blue circles.

field 1 involved the same steps previously described in Section 3.2. We selected 250 probable YSO candidates out of 33 676 objects identified in UKIDSS DR6. For the SED analysis, we used the same A_V ranges and distances. As a result, we obtained relatively robust parameters for *only* 12 objects with $\chi^2 < 100$.

The stellar content analysis of Control field 1 allows us to conclude that the 431 YSOs ($\chi^2 < 100$) selected by the SED fitting tool in our considered region are located with high probability at the same distance as two UCHII regions. By examining the distances corresponding to the models obtained with the SED fitting tool, we found that, for most objects, the best models correspond to a distance of 7.8 kpc. For the other 45% of the objects, the SED fitting tool did not yield a reliable result. In addition to the aforementioned reasons, this issue may relate to the presence of fore/background objects. The latter issue is especially likely because the region is distant.

3.4. Final catalogue

As noted earlier, we included objects in the initial UKIDSS DR6 selection with the catalogue parameter mergedClass = +1 (galaxy) and -3 (probable galaxy). Among these, there may be some artefacts or so-called non-stellar objects (Solin, Ukkonen, & Haikala 2012). The reasons for their formation may be manifold, including nebulous structures, diffraction patterns of bright stars, bright stars at or near the border of the detector array, etc. To justify the reliability of the final list, we reviewed our sample for artefacts. For this purpose, following the advice of previous works (e.g. Lucas et al. 2008; Solin et al. 2012), the parameter k_1ppErrBits was used. This parameter contains the quality error information for each source detected by the K filter. Among the 431 objects with robust SEDs, only one showed k_1ppErrBits = 64 (i.e. bad pixel(s)) and seven showed k_1ppErrBits = 4 194 304 (i.e. lies within a dither offset of the stacked frame boundary); we thus excluded these from the final list. Such a small percentage of artefacts (~2%) indicates sufficiently reliable filtering of stellar objects using the SED fitting tool.

We also performed a visual inspection of the 115 YSO candidates that were selected based only on their NIR photometric

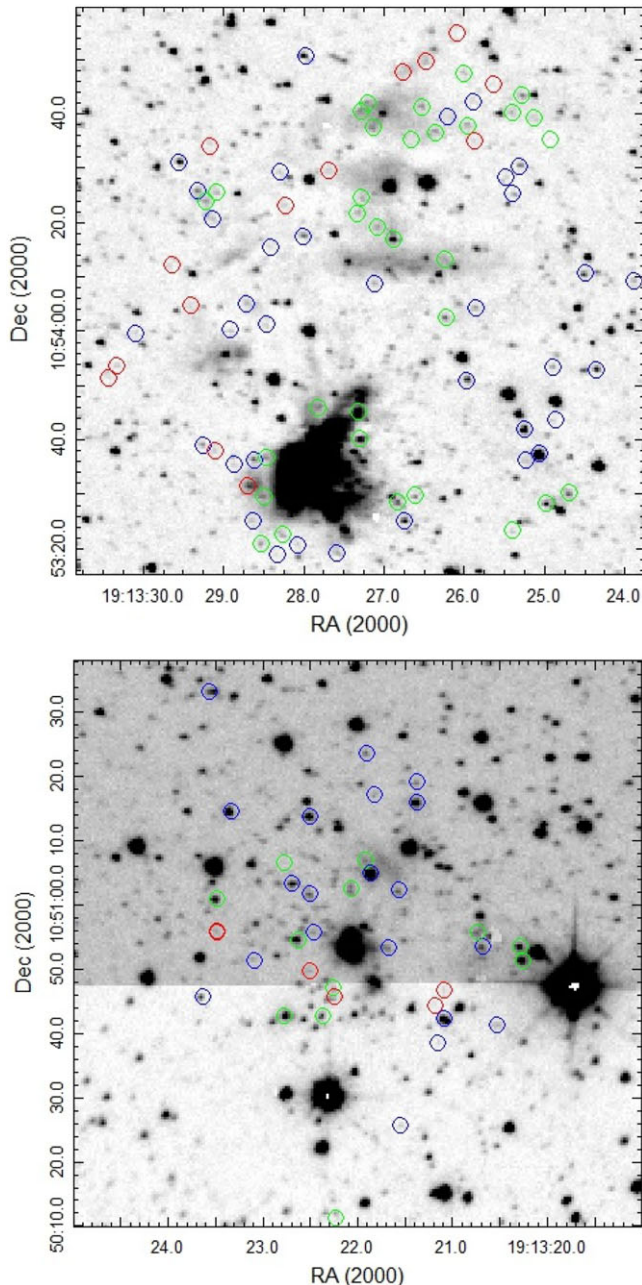


Figure 7. K image of G45.07+0.13 (top panel) and G45.12+0.13 (lower panel). The selected YSOs with mergedClass = -1/-2 (star/probable star marked by blue circles, mergedClass = +1/-3 (galaxy/probable galaxy) - by green circles. Red circles show the identified non-stellar objects.

data. From our point of view, these objects are of the greatest interest as they are located in the immediate vicinity of the UCHIIIs. The analysis results are shown in Figure 7. The surface brightness distribution of 20 faint objects indicates that they can be attributed to extended/non-stellar objects rather than point sources. In UKIDSS DR6, they were identified as galaxies/probable galaxies (mergedClass = +1/-3). These objects are marked with red circles in Figure 7. To ensure the purity of the sample, we removed these objects from the final list.

Overall, the final list comprised 518 YSOs (423 with constructed SEDs and 95 YSOs in two saturated regions). The

coordinates, NIR and MIR photometric data, α_{IRAC} , and evolutionary stage of the 518 YSOs are presented in Table NIR,^a while Table FIR^b presents the FIR fluxes of the selected objects. In total, we identified 23 objects in FIR bands, including the object associated with IRAS 19111+1048. Table SED^c shows the weighted means and the standard deviation values of parameters for all models with $\chi^2 - \chi_{best}^2 < 3N$ obtained by the SED fitting tool. In Tables NIR, FIR, and SED, the parameters of the members of the region are listed in the following order: first, the IRAS 19111+1048 source then objects within the IRAS 19111+1048 and IRAS 19110+1045 clusters (see Section 3.5), and, finally, those within a 6 arcmin radius of the whole region that are not included in the clusters. The numbering of objects in Table SED was performed according to Tables NIR and FIR. Table SED contains the parameters of the 423 objects for which the SED fitting tool achieved a value of $\chi^2 < 100$.

Some conclusions can be drawn based on the data obtained by the SED fitting tool. The average interstellar extinction value is equal to $A_v=13$ mag, which corresponds to a lower interstellar extinction estimate than that obtained from the COBE/DIRBE and IRAS/ISSA maps (Schlegel et al. 1998). The average mass of the YSOs is approximately $4.4 M_{\odot}$, with a minimum estimated mass of $1.7 M_{\odot}$ and a maximum of $22 M_{\odot}$. Primarily, the lack of low-mass stellar objects can be explained by the large distance of the star-forming region.

3.5. Distribution of YSOs

The top panel of Figure 8 shows the distribution of the selected YSOs in the field, with Class I and Class II objects shown by filled red and blue circles, respectively. Excluding the regions in the vicinity of the IRAS sources, all types of stellar objects are distributed relatively homogeneously in the molecular cloud. Additionally, in both UCHII regions, close to the IRAS sources, the selected YSOs form relatively dense concentrations or clusters. These concentrations were revealed above by the radial distribution of stellar densities (see Section 3.2.1 and Figure 4). The existence of the cluster around IRAS 19111+1048 is more obvious now. We refined the radius of each cluster relative to its geometric centre based on the density distribution of the selected YSOs. The stellar density was determined for each ring of width $0.1'$ by dividing the number of YSOs by the surface area. The radius of each cluster was considered the distance at which fluctuations in the rings' stellar density became random according to Poisson statistics. Table 2 presents the coordinates of the geometric centres of the clusters in the vicinity of IRAS sources and the whole region in Cols. 2 and 3, the coordinates of IRAS sources in Cols. 4 and 5, and the radii of the clusters in Col. 6. Cols. 7 and 8 present the stellar content and surface density of each cluster, as well as of the whole region, based on our selection. The surface density of stars in clusters is four times higher than that of the entire region. The radii of the clusters are in good agreement with the sizes of the UCHII regions as determined by the distributions of dust temperature and column density (see Section 3.1). Note that in previous studies, the young massive (OB) population embedded in the innermost regions of the clump has already been reported (e.g. Vig et al. 2006; Rivera-Ingraham et al. 2010). The two insets in

^a Available online.

^b Available online.

^c Available online.

Table 2. Properties of the region.

Name	$\alpha(2000)$ (hh mm ss)	$\delta(2000)$ (dd mm ss)	$\alpha(2000)$ (hh mm ss)	$\delta(2000)$ (dd mm ss)	Radius (arcmin)	N	Density (arcmin ⁻²)
(1)	(2)	(3)	(4)	(5)	(6)	(7)	(8)
IRAS 19111+1048	19 13 27.8	+10 53 36.74	19 13 27.3	+10 54 07.42	1.2	87	19.2
IRAS 19110+1045	19 13 22.0	+10 50 54.00	19 13 23.1	+10 50 51.88	0.8	37	18.4
Region	—	—	19 13 24.2	+10 53 38.00	6	518	4.6

Notes. (1)—names of (sub-)regions, (2),(3)—coordinates of the IRAS sources, (4),(5)—coordinates of the geometric centres, (6)—the radii of (sub-)regions, (7)—numbers of objects within the selected radii, (8)—surface stellar density in the (sub-)regions.

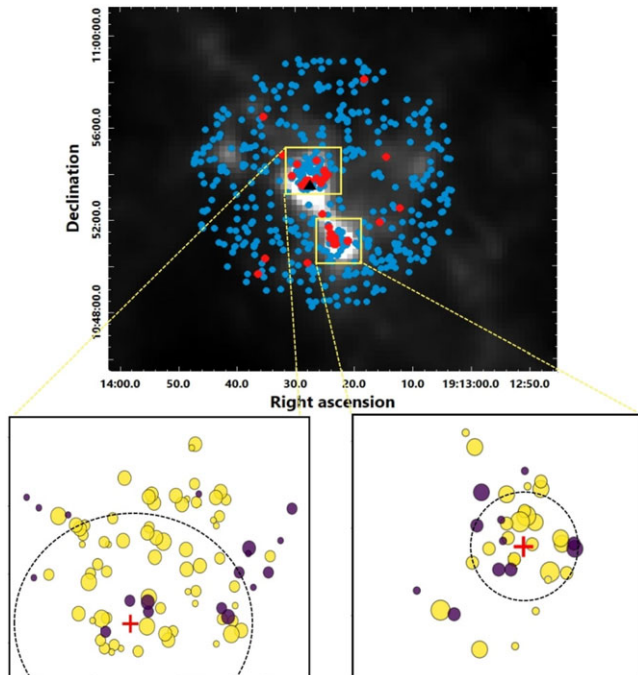


Figure 8. (Top panel): Distribution of YSOs in the region on *Herschel* 500 μm image. Class I and Class II objects are indicated by filled red and blue circles, respectively. IRAS 19111+1048 source is indicated by a black triangle. (Bottom panels): The two insets show the distribution of the clusters' members. Yellow and purple circles correspond to an older and younger population, respectively. The size of each circle is related to its mass falling within certain interval of masses: 1–3 M_{\odot} (smallest), 3–5 M_{\odot} , 5–7 M_{\odot} , > 7 M_{\odot} (largest). The colour and size of the members are taken based on their positions on the CMD (Figure 9 left panel). Red crosses show the coordinates of IRASs. Dashed circles shows the MIR-saturated regions around the IRAS sources.

the lower panels of Figure 8 show the distribution of the members in the dense clusters. The yellow and purple circles correspond to older and younger populations, respectively. The size of each circle is related to its mass falling within certain mass intervals: 1–3 M_{\odot} (smallest), 3–5 M_{\odot} , 5–7 M_{\odot} , and > 7 M_{\odot} (largest). The colour and size of the members are taken based on their positions on the CMD (see Figure 9 left panel). The surface density distribution of the YSOs did not show any concentration around the BGPS 6737 (MSX G045.1663+00.0910) object.

Vig et al. (2006) proposed that the initial trigger and power source of G45.12+0.13 is the brightest radio source S14, which was deduced to be of spectral type O6 from integrated radio emission. They also found two NIR objects, IR4 and IR5, within S14. According to our data, the nearest object to the S14 peak ($\sim 7.7''$) that can satisfy the conditions defined in Vig et al. (2006) is a star with $9.4 \pm 4.3 M_{\odot}$ mass, $23\,000 \pm 11\,000$ K temperature,

and $(2.5 \pm 1.2) \times 10^6$ years evolutionary age. This star is mentioned as IRAS 19111+1048 in Tables *NIR*, *FIR*, *SED*, and the NIR c-c diagram. It is also the closest object ($\sim 9''$) to the brightest source A16-24 obtained by the CORNISH interferometer at 4.8 GHz (Rivera-Ingraham et al. 2010). This stellar object has II evolutionary class. Besides IRAS 19111+1048 source, two selected YSOs are also located within the radio contours of S14, i.e. stars ID 52 and 53 in Table *NIR*, which are located at distances about 8.5 and 11'' from the S14 peak, respectively. This group of objects can be assumed to be the power source of G45.12+0.13. Liu et al. (2019) also suggested that S14 is a protocluster hosting several ZAMS stars.

According to Vig et al. (2006), IRAS 19110+1045 is associated with the compact radio source S27, which has no NIR counterparts. Using the SED fitting tool, Persi & Tapia (2019) obtained embedded pair of YSOs with the mass of 24 M_{\odot} associated with IRAS 19110+1045. Unfortunately, due to the saturation of the central parts of UC HII regions in the MIR range, we were unable to identify the YSOs associated with this source.

We examined the location of identified stellar objects in relation to radio sources (Vig et al. 2006; Rivera-Ingraham et al. 2010). Table 3 includes objects that are located no further than 5'' from the peak of the radio sources. For the majority, we see that at least one stellar object can be associated with a radio source from Vig et al. (2006).

3.6. Colour-magnitude diagram

A colour-magnitude diagram (CMD) is a useful tool to study the nature of the stellar population within star-forming regions. The K versus $J-K$ diagram provides the maximum contrast between the IR excess produced by the presence of a disc, which mostly affects K , and interstellar extinction, which has a greater effect on J . The distribution of the identified YSOs in the K versus $J-K$ CMD is shown in the left panel of Figure 9. The ZAMS (thick solid curve) and PMS isochrones for the 0.1 and 1 Myr ages (thin solid curves) are taken from Siess et al. (2000). We used the conversion table from Kenyon et al. (1994). Circles indicate stars in the IRAS clusters, while red circles are stars with more than three photometric measurements. For these stars, the SED fitting tool obtained reliable parameters (i.e. $\chi^2 < 100$). Yellow circles represent objects in the saturated regions that have only three photometric measurements. Objects located outside of the two IRAS clusters (hereafter *non-cluster*) for which the SED fitting tool obtained reliable parameters are marked by blue crosses. The black dots are objects with no reliable parameters ($\chi^2 > 100$). To correct the J and K magnitudes of the selected YSOs, we used a 7.8 kpc distance and the average interstellar extinction value ($A_v = 13$ mag, see Section 3.3). NIR excess, shown in the c-c diagrams

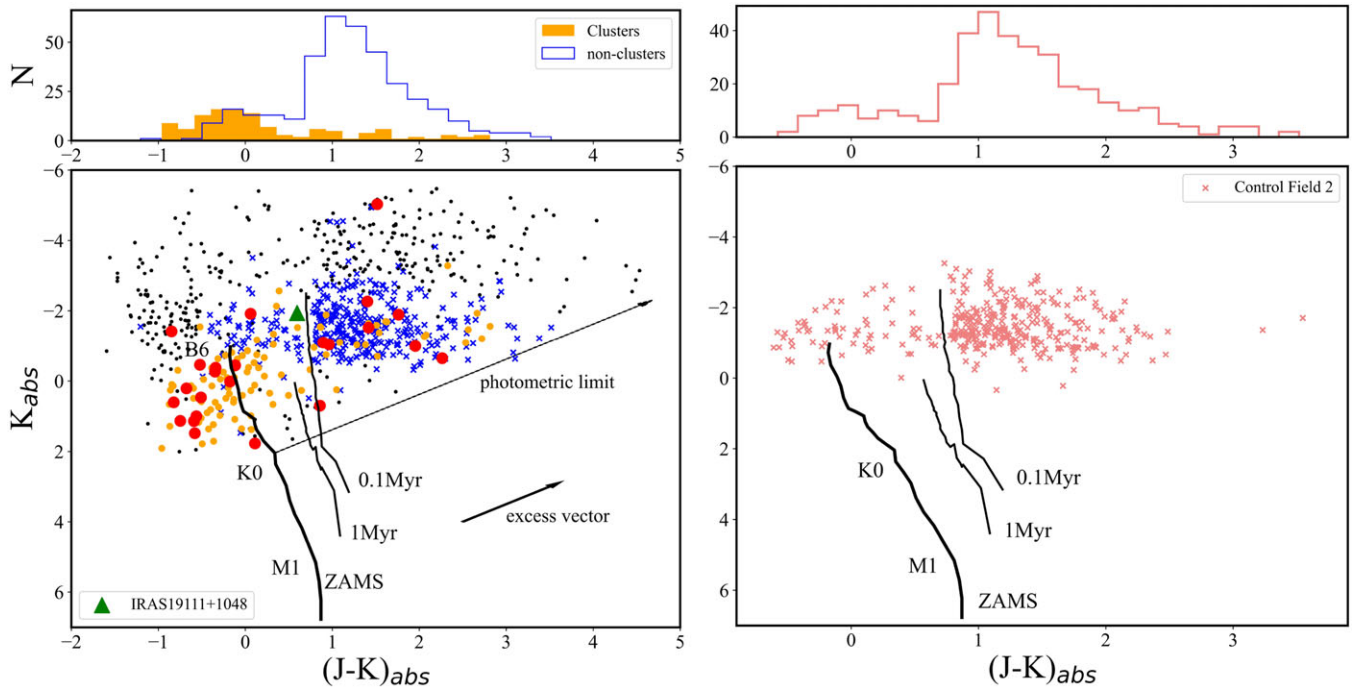


Figure 9. K versus $(J-K)$ colour-magnitude diagrams for identified YSOs in the considered region (*bottom left panel*) and Control field 2 (*bottom right panel*). The PMS isochrones for the 0.1 and 1 Myr (Siess, Dufour, & Forestini 2000) and ZAMS are drawn as solid thin and thick lines, respectively. The positions of a few spectral types are labelled. The J and K magnitudes of the YSOs are corrected for the interstellar extinctions determined according to average $A_v = 13$ mag value obtained by the SED fitting tool. (*bottom left panel*): Red circles are stellar objects within the IRAS clusters with constructed SED based on more than 3 photometric data points. Objects located in the saturated regions around two IRAS sources are yellow circles. Non-cluster objects are blue crosses and no-SED objects are black dots. IRAS 19111+1048 source is indicated by a green triangle and labelled. The solid arrow indicates the average slope of NIR excesses caused by circumstellar discs (López-Chico & Salas 2007). The dashed arrow indicates the photometric limit of UKIDSS in K -band. (*bottom right panel*): Stellar objects located in Control field 2 are indicated by coral crosses. (*Top left and right panels*): Histograms of $(J-K)_{abs}$ values.

(Figure 5), is usually caused by the presence of disks around young stars; thus, by incorporating theoretical accreting disk models, the excess effect on the CMD can be accurately represented by vectors of approximately constant slope for disks around Class II T Tauri stars. The components of the vector are (1.01, -1.105) and (1.676, 1.1613) in magnitude units (López-Chico & Salas 2007). More massive YSOs are usually much more embedded than T Tauri stars, thus, this correction is unlikely to apply to such objects. However, the presence of a spherical envelope around the disc should cause a greater decrease in $J-K$ for the same variation in the K than in the case of a ‘naked’ disc (Cesaroni et al. 2015); accordingly, the López-Chico & Salas (2007) correction can be used to obtain a lower limit of stellar mass in the region. Using the excess vector, we also determined the photometric limit of the UKIDSS data represented by the dashed arrow in the diagram; this is parallel to the excess vector and passes through the ZAMS point with coordinates (0.34, 2.05). The Y -coordinate corresponds to the photometric limit of UKIDSS in the K band (18.02 mag) corrected for distance and interstellar extinction. The photometric limit corresponds to the ZAMS stars with $1.4 M_{\odot}$ mass; this value is in good agreement with the minimum mass (i.e. $1.7 M_{\odot}$), obtained by the SED fitting tool. We observe that all detected objects are brighter in the K -band than the photometric limit of the UKIDSS survey. Undoubtedly, the large distance and interstellar extinction play a crucial role in this result.

Several conclusions can be drawn based on the location of stellar objects in the CMD. Objects without reliable parameters (black dots) occupy a separate region; in general, these are brighter in the K -band than objects with reliable parameters and most of

Table 3. Comparison of IR and radio data.

ID	GMRT	CORNISH	ID	GMRT	CORNISH
(1)	(2)	(3)	(1)	(2)	(3)
10	S3	—	63, 68	S18	—
11	S6	—	64	—	A16–C32
16	S5	—	65, 71	S16	—
26, 36	S10	—	66	—	A16–C33
37	S9	—	74	S19	—
43, 45	S12	—	87, 88	S24	—
50, 53	—	A16–C8	91	S25	—
56	—	A16–C25	98	S27	A12–C1
58	S15	—	120	—	A16–C5
59, 60	—	A16–C27	105	—	A12–C3

Notes. (1)—ID of objects from Table NIR, (2)—sources obtained by radio continuum observations at 1 280, 610 MHz frequency bands (Vig et al. 2006), (3)—sources obtained by CORNISH interferometer at 4.8 GHz (Rivera-Ingraham et al. 2010).

them are likely foreground objects. The stars that belong to the star-forming region (circles and crosses) have considerable variation concerning their colour index, i.e. $(J-K)_{abs}$. The positions of objects in the two IRAS clusters and non-cluster regions are different. An overwhelming majority (more than 80%) of the non-cluster objects are located to the right of the 0.1 Myr isochrone. In contrast, about 75% of objects in the IRAS clusters are located to the left of the 0.1 Myr isochrone and concentrated around the ZAMS, some of which fall to the left of the ZAMS. For improved

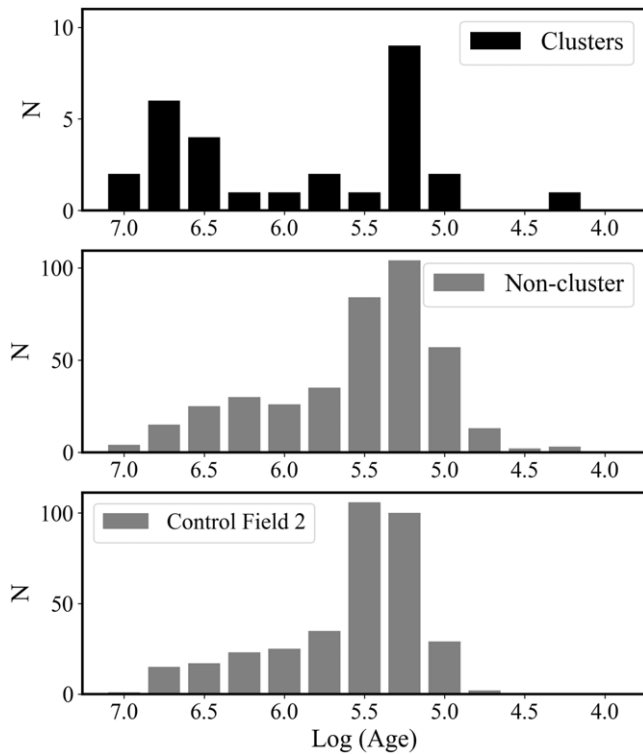


Figure 10. Histogram of evolutionary ages (by the SED fitting tool) for members of the IRAS clusters (top panel), the non-cluster objects (middle panel), and the objects in the Control field 2 (bottom panel). The bin size corresponds to $\text{Log}(\text{Age}) = 0.25$.

clarity, the histograms of $(J - K)_{\text{abs}}$ are shown in the top panels of Figure 9. In general, the evolutionary age spread of the vast majority of stellar objects from both samples is small; furthermore, the members of the IRAS clusters are more developed than the non-cluster objects.

The middle panel of Figure 10 shows the distribution of evolutionary ages (by the SED fitting tool) for the non-cluster objects, which confirms the above interpretation. The age distribution of these objects has a well-defined peak at $\text{Log}(\text{Age}) \approx 5.25$. In contrast, the distribution of the evolutionary ages of the objects in the clusters has two peaks (Figure 10 top panel) centred at $\text{Log}(\text{Age}) \approx 6.75$ and $\text{Log}(\text{Age}) \approx 5.25$. Note that the age distribution of the objects in the clusters was constructed based on parameters from only 29 YSOs for which the SED fitting tool was applied. Most of the other 95 YSOs in the MIR-saturated regions are concentrated around the ZAMS and to the left of the 1 Myr isochrone. Therefore, we assume that these objects will have a real contribution to the first peak in the evolutionary age distribution. Accordingly, this distribution will have only one well-defined peak as per the histogram of $(J - K)_{\text{abs}}$ around $\text{Log}(\text{Age}) \approx 6.75$.

The cluster identification confirms the assumptions made in previous studies based mainly on radio observations of star clusters near the IRAS sources, which include high- and intermediate-mass ZAMS objects (e.g. Liu et al. 2019; Rivera-Ingraham et al. 2010; Vig et al. 2006, and ref. therein). The clusters' members exhibit low scatter relative to the isochrones. The clusters' origin can be assumed to relate to an external triggering shock. We examined the distribution of the cluster members relative to their masses and evolutionary ages (see the lower panels of Figure 8), which demonstrated that the objects are not segregated according

to these parameters. The members of the IRAS 19111+1048 cluster are asymmetrically arranged relative to the IRAS source, and, like the isotherms (see Figure 3), are elongated in a northwest direction. There are potentially two UCHII regions herein (i.e. G45.12+0.13 and G45.13+0.14) that are separated from each other in a northwest direction (de la Fuente et al. 2020a).

The non-cluster objects of all evolutionary classes are uniformly distributed across the field (see Figure 8 top panel). As shown in previous studies, several massive stellar objects in or near the ZAMS are responsible for the ionisation of UC HII regions and can trigger a second star formation event along the ionising radiation ridge (e.g. Blum & McGregor 2008; Paron, Cichowolski, & Ortega 2009). Accordingly, the newly formed stars are unevenly distributed and localised in the radiation ridge. In our study, the non-cluster YSOs are found to be uniformly distributed in the molecular cloud. Therefore, the origin of the non-cluster objects cannot be explained by the activity of the embedded massive stars in the UCHII regions. We instead assume that these uniformly distributed objects are part of the young stellar population of the GRSMC 45.46+0.05 molecular cloud, which is an active star-forming region (Simon et al. 2001).

To confirm this assumption, we performed the same analysis in Control field 2, an area we selected that is located in the GRSMC 45.46+0.05 star-forming region and very close to the considered region. Figure 6 shows the position of Control field 2 with the same 6 arcmin radius. The analysis of the stellar population of Control field 2 includes the same steps described in Section 3.2. We selected 777 YSO candidates out of 30 254 objects identified in UKIDSS DR6. For the SED analysis of these YSO candidates, we used the same A_V and distance ranges of 10–100 mag and 6.5–9.5 kpc, respectively. We obtained relatively robust parameters for ~ 350 objects ($\chi^2 < 100$); therefore, the number of YSOs in Control field 2 is almost the same as the number of non-cluster objects in the considered region. The mass range of these objects also coincides (from 1.9 to 18 M_{\odot}). The evolutionary age distributions of the non-cluster stellar objects and Control field 2 objects show significant similarity (see bottom panel of Figure 10), with the Control field 2 object ages exhibiting one well-defined peak. The distribution of evolutionary ages and the peak value ($\text{Log}(\text{Age}) \approx 5.35$) coincide with those of the non-cluster objects. To further confirm the similarity between the non-cluster and Control field 2 stellar objects, we also used CMD. The distribution of the objects from Control field 2 in the K versus $J - K$ CMD is shown in the right panel of Figure 9 (coral crosses). We used the same correction as previously for the J and K photometry, i.e. 7.8 kpc distance and $A_V = 13$ mag interstellar extinction. More than 80% of the objects are located to the right of the 0.1 Myr isochrone, like the non-cluster objects. Thus, the main parameters (evolutionary ages, masses, and surface stellar density) of the non-cluster and Control field 2 objects are almost the same. Accordingly, our assumption that the non-cluster YSOs are part of the young stellar population of the GRSMC 45.46+0.05 molecular cloud is plausible. To understand the tracers of their origins, the star formation history of the GRSMC 45.46+0.05 star-forming region as a whole must be investigated.

3.7. K luminosity function and initial mass function

The luminosity function in the K -band is frequently used in studies of young clusters and star-forming regions as a diagnostic tool of their IMF and the star formation history of their stellar

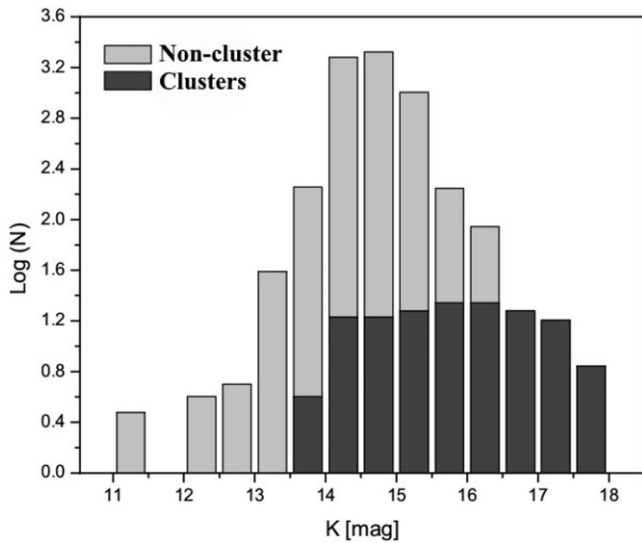


Figure 11. K luminosity functions derived for the IRAS clusters (dark grey) and non-cluster objects (light grey) as histograms of the number of stars in logarithm versus apparent K magnitude. The bin size corresponds to 0.5 mag.

populations (Zinnecker et al. 1993; Lada & Lada 1995; Jose et al. 2012). The observed KLF is a result of the IMF, PMS evolution, and star-forming history; thus, the KLF slope is a potential age indicator of young clusters (Lada, Alves, & Lada 1996). The KLF can be defined as $dN(K)/dK \propto 10^{\alpha K}$, where α is the slope of the power law and $N(K)$ is the number of stars brighter than K mag. We evaluated the α slopes individually for the stellar populations of the IRAS clusters and the non-cluster objects. The KLF slopes were estimated by fitting the number of YSOs in 0.5 mag bins using a linear least-squares fitting routine. Since the interstellar extinction is independent of stellar mass, it does not affect the result (Megeath et al. 1996); therefore we can use all the sources in the sample to define the slopes without the complication of extinction correction. Figure 11 shows the observed overplotted KLFs of the IRAS clusters (dark grey) and the non-cluster objects (light grey). No sharp decline is recorded at the end of KLF as a whole, i.e. it occurs gradually, showing that the photometric completeness limit of the survey did not strongly affect the shape of the KLF. Note that the KLF of the IRAS clusters does not show an obvious maximum while the KLF of the non-cluster objects has a maximum at the same magnitude as the whole region. This is most likely due to the quantitative ratio between the objects from different samples. Its slope is also noticeably steeper than that of the IRAS clusters' KLF. Thus, the IRAS clusters appear to show unique characteristics relative to the whole region, once again confirming that they are at different stages of evolution. The calculated KLF α slopes for the IRAS clusters and non-cluster objects were 0.23 ± 0.10 and 0.55 ± 0.09 , respectively.

One of the most fundamental disciplines of astrophysical research is the origin of stars and stellar masses. The IMF, together with the star formation rate, dictates the evolution and fate of both galaxies and star clusters (Kroupa 2002). The study of the IMFs of star-forming regions is important—their mass functions (MFs) can be considered as IMFs because they are too young to lose a significant number of members through dynamical or stellar evolution effects. We assume that the MF and the mass-luminosity relation for a stellar cluster are described by power laws like the KLF, i.e. they are of the form $dN(\log m) \propto m^\gamma$ and $L_K \propto m^\beta$, where

γ and β are the slopes of MF and mass-luminosity relation, respectively. We obtained two completely different KLF results for the two IRAS clusters and the non-cluster objects. Here, we discuss the IMF of each case separately as the initial conditions may differ. The mass-luminosity relation with $\beta \sim 1$ is mostly used for stars at the lower mass end of the IMF, i.e. G–M stars for the 1 Myr cluster (Lada, Young, & Greene 1993; Megeath et al. 1996). If $\beta \sim 1$, values such as $\alpha = \gamma/(2.5\beta) = 0.68$ and 0.54 would be expected for power-law IMFs with slopes $\gamma = 1.7$ (Miller & Scalo 1979; Scalo 1986) and 1.35 (Salpeter 1955), respectively. The latter value is in good agreement with our KLF fit result for the non-cluster stellar objects (0.55 ± 0.09). If we assume $\beta \sim 2$, typically used for a larger and higher mass range (O–F stars) at 1 Myr (Balog et al. 2004), this results in $\alpha = 0.27$ for a Salpeter-type IMF and $\alpha = 0.34$ for a Miller-Scalo type IMF. The Salpeter-type IMF is closer to the KLF fit result for the two IRAS clusters (0.23 ± 0.10). The results obtained via the IMFs are well-correlated with the masses obtained from the SED fitting tool (see Section 3.3). Notably, the 1 Myr age estimate for the non-cluster objects does not match with the results of the SED fitting tool and CMD (see Figures 10 and 9)—in general, the non-cluster objects are noticeably younger. Such a discrepancy is because the mass-luminosity relation with $\beta \sim 1$ is used mostly for low-mass stars, while the SED fitting tool did not find any low-mass objects in the region and the CMD shows that the photometric limit of UKIDSS in the K -band influenced the detection of faint objects in the region. Thus, the resulting loss of low-mass YSOs in the region will strongly affect the results of the star formation rate and star formation efficiency calculation, so we did not define these parameters.

4. Summary and conclusions

An infrared study of the star-forming region in a molecular cloud, which includes the UCHII regions G45.12+0.13/IRAS 19111+1048 and G45.07+0.13/IRAS 19110+1045, was undertaken with two major components: (i) determination of the ISM physical parameters (i.e. $N(\text{H}_2)$ and T_d) and (ii) searching for and studying the young stellar population.

To determine $N(\text{H}_2)$ and T_d , we applied modified blackbody fitting on *Herschel* images obtained in four bands: 160, 250, 350, and 500 μm . The maps of these parameters allowed us to conclude:

- Within the G45.07+0.13 and G45.12+0.13 regions, $N(\text{H}_2)$ varies from $\sim 3.0 \times 10^{23}$ to $5.5 \times 10^{23} \text{ cm}^{-2}$.
- The T_d maximum in G45.12+0.13 is 35 K and in G45.07+0.13 it is 42 K.
- The dust temperature drops significantly from the centre to the periphery, reaching values of around 18–20 K. The T_d decline levels out at distances of ~ 2.6 and ~ 3.7 pc from IRAS 19110+1045 and IRAS 19111+1048, respectively. The masses of the gas-dust matter are $\sim 1.7 \times 10^5 M_\odot$ and $\sim 3.4 \times 10^5 M_\odot$ in the G45.07+0.13 and G45.12+0.13 regions, respectively.
- The column density map revealed a bridge between the two UCHII regions with relatively high density ($N(\text{H}_2) = 4.3 \times 10^{23} \text{ cm}^{-2}$) and low temperature ($T_d = 19$ K), which is also clearly visible on *Herschel* images. This suggests that these two UCHII regions are physically connected.

The objectives of studying the stellar population were to identify the members of the clusters, associated with the UC HII regions, as well as to determine their main parameters (e.g. stellar masses, evolutionary ages, and age spread). The identification and classification of YSOs using NIR, MIR, and FIR photometric data were based on one of the main properties of young stars, namely, their infrared excess due to the presence of circumstellar discs and envelopes. The SED fitting tool (Robitaille et al. 2006) was used to determine their main parameters. Within a 6 arcmin radius around the UC HIIs, we obtained relatively robust parameters for 423 YSOs (16 Class I and 407 Class II objects) with $\chi^2 < 100$. We also identified 95 YSOs located in the two MIR-saturated regions based only on the *J*, *H*, and *K* photometric data. A detailed study of stellar objects in the considered star-forming region made it possible to obtain the following results:

- The stellar density radial distribution shows the existence of dense clusters in the vicinity of both IRAS sources. These clusters include 37 and 87 members in G45.07+0.13 and G45.12+0.13, respectively. Their surface stellar density exceeds the average over the star-forming region around four-fold. The radii are in good agreement with the sizes of the UC HII regions as determined by the distributions of dust temperature and column density. The remaining 394 non-cluster objects, irrespective of their evolutionary classes, are uniformly distributed in the molecular cloud.
- We were unable to identify stellar objects with masses less than $1.4 M_{\odot}$. This can be explained by the large distance of the star-forming region.
- The study of the stellar parameters from different samples (i.e. clusters and non-cluster) showed differences between the two populations.
- On the CMD, around 75% of the YSOs in the IRAS clusters are located to the left of the 0.1 Myr isochrone and are concentrated around the ZAMS. The slope α of the KLF for these objects is 0.23 ± 0.10 , which agrees well with a Salpeter-type IMF ($\gamma = 1.35$) for a high mass range (O–F stars, $\beta \sim 2$) at 1 Myr.
- The detailed study of the clusters made it possible to identify the stellar object associated with IRAS 19111 +1048, and this can be the exciting star of G45.12+0.13. This is a star with $9.4 \pm 4.3 M_{\odot}$ mass, $23\,000 \pm 11\,000$ K temperature, and $(2.5 \pm 1.2) \times 10^6$ yr evolutionary age.
- The median value of the evolutionary ages obtained by the SED fitting tool for the non-cluster objects is $\text{Log}(\text{Age}) \approx 5.25$, more than 80% of which are located to the right of the 0.1 Myr isochrone. The slope α of the KLF for these objects is 0.55 ± 0.09 , which agrees better with a Salpeter-type IMF for low-mass objects (G–M stars, $\beta \sim 1$).

Based on the results, we concluded that dense clusters were formed in both UC HII regions, which include high- and intermediate-mass stellar objects. The evolutionary ages of these stars, in most cases, are several million years. Likely, low-mass stellar objects were not identified due to the large distance of the star-forming region. The small spread of evolutionary ages suggests that the clusters owe their origin to a triggering shock. Presumably, the low-density extended emission observed on the MIR images (de la Fuente et al. 2020a), which also stands out well

on the dust temperature maps in both UC HII regions, may be due to the existence of the stellar clusters.

The distribution of the non-cluster objects in the molecular cloud implies that their origin cannot be explained by the activity of the embedded massive star(s) in the UC HII regions. We assume that these uniformly distributed objects are part of the young stellar population of the GRSMC 45.46+0.05 molecular cloud, which is an active star-forming region. To understand the tracers of their origins, it is necessary to investigate the star formation history of the GRSMC 45.46+0.05 star-forming region as a whole. This extended star-forming region, spreading over an area of about 6 deg^2 in Aquila, is known to host numerous UC HII regions, maser emissions, and outflows from young and highly embedded OB stellar clusters (e.g. Simon et al. 2001; Rivera-Ingraham et al. 2010). This work is a part of the project to study the UC HII regions in GRSMC 45.46+0.05, and, consequently, massive star formation and its influence on the surrounding ISM.

Acknowledgement. We thank the anonymous reviewer for constructive comments and suggestions. We thank Lex Kaper for carefully reading the manuscript and for his helpful remarks. This work was made possible by a research grant number N° 21AG–1C044 from Science Committee of Ministry of Education, Science, Culture, and Sports RA. This research has made use of the data obtained at UKIRT, which is supported by NASA and operated under an agreement among the University of Hawaii, the University of Arizona, and Lockheed Martin Advanced Technology Centre; operations are enabled through the cooperation of the East Asian Observatory. We gratefully acknowledge the use of data from the NASA/IPAC Infrared Science Archive, which is operated by the Jet Propulsion Laboratory, California Institute of Technology, under contract with the National Aeronautics and Space Administration. We thank our colleagues in the GLIMPSE and MIPSGAL *Spitzer* Legacy Surveys. This publication also made use of data products from *Herschel* ESA space observatory.

References

- Allen, L., et al. 2007, *Protostars and Planets V*, 361
 Allen, L. E., et al. 2004, *ApJS*, **154**, 363
 Argon, A. L., Reid, M. J., & Menten, K. M. 2000, *ApJS*, **129**, 159
 Azatyan, N. M. 2019, *A&A*, **622**, A38
 Azatyan, N. M., Nikoghosyan, E. H., & Khachatryan, K. G. 2016, *Ap*, **59**, 339
 Balog, Z., et al. 2004, *AJ*, **128**, 2942
 Battersby, C., et al. 2011, *A&A*, **535**, A128
 Bessell, M. S., & Brett, J. M. 1988, *PASP*, **100**, 1134
 Blum, R. D., & McGregor, P. J. 2008, *AJ*, **135**, 1708
 Breen, S. L., et al. 2019, *MNRAS*, **484**, 5072
 Carey, S. J., et al. 2009, *PASP*, **121**, 76
 Carpenter, J. M. 2001, *AJ*, **121**, 2851
 Caulet, A., Gruendl, R. A., & Chu, Y. H. 2008, *ApJ*, **678**, 200
 Cesaroni, R., et al. 2015, *A&A*, **581**, A124
 Churchwell, E. 2002, *ARA&A*, **40**, 27
 Churchwell, E., Sievers, A., & Thum, C. 2010, *A&A*, **513**, A9
 Churchwell, E., Walmsley, C. M., & Wood, D. O. S. 1992, *A&A*, **253**, 541
 Churchwell, E., et al. 2009, *PASP*, **121**, 213
 de la Fuente, E., et al. 2020a, *MNRAS*, **492**, 895
 de la Fuente, E., et al. 2020b, *MNRAS*, **497**, 4436
 Egan, M. P., et al. 2003, *VizieR Online Data Catalog*, 5114
 Ellsworth-Bowers, T. P., et al. 2015, *ApJ*, **799**, 29
 Elmegreen, B. G., & Lada, C. J. 1977, *ApJ*, **214**, 725
 Fazio, G. G., et al. 2004, *ApJS*, **154**, 10
 Fish, V. L., Reid, M. J., Wilner, D. J., & Churchwell, E. 2003, *ApJ*, **587**, 701
 Flaherty, K. M., et al. 2007, *ApJ*, **663**, 1069
 Garay, G., & Lizano, S. 1999, *PASP*, **111**, 1049

- Griffin, M. J., et al. 2010, *A&A*, **518**, L3
- Gutermuth, R. A., et al. 2008, *ApJ*, **674**, 336
- Han, X. H., et al. 2015, *A&A*, **576**, A131
- Hartmann, L. 2009, *Accretion Processes in Star Formation* (2nd edn.; Cambridge University Press)
- Hartmann, L., et al. 2005, *ApJ*, **629**, 881
- Hernández, J., et al. 2005, *AJ*, **129**, 856
- Hernández-Hernández, V., et al. 2019, *AJ*, **158**, 18
- Hernández-Hernández, V., Zapata, L., Kurtz, S., & Garay, G. 2014, *ApJ*, **786**, 38
- Hildebrand, R. H. 1983, *QJRAS*, **24**, 267
- Hofner, P., & Churchwell, E. 1996, *A&AS*, **120**, 283
- Hunter, T. R., Phillips, T. G., & Menten, K. M. 1997, *ApJ*, **478**, 283
- Jose, J., et al. 2012, *MNRAS*, **424**, 2486
- Kauffmann, J., Bertoldi, F., Bourke, T. L., Evans, N. J., I., & Lee, C. W. 2008, *A&A*, **487**, 993
- Kenyon, S. J., Gomez, M., Marzke, R. O., & Hartmann, L. 1994, *AJ*, **108**, 251
- Keto, E. 2007, *ApJ*, **666**, 976
- Koenig, X. P., et al. 2012, *ApJ*, **744**, 130
- Könyves, V., et al. 2015, *A&A*, **584**, A91
- Kroupa, P. 2002, *Sci*, **295**, 82
- Kurtz, S., Churchwell, E., & Wood, D. O. S. 1994, *ApJS*, **91**, 659
- Lada, C. J. 1987, in *IAU Symposium*, Vol. 115, *Star Forming Regions*, ed. M. Peimbert, & J. Jugaku, **1**
- Lada, C. J., & Adams, F. C. 1992, *ApJ*, **393**, 278
- Lada, C. J., Alves, J., & Lada, E. A. 1996, *AJ*, **111**, 1964
- Lada, C. J., & Lada, E. A. 2003, *ARA&A*, **41**, 57
- Lada, C. J., Young, E. T., & Greene, T. P. 1993, *ApJ*, **408**, 471
- Lada, C. J., et al. 2006, *AJ*, **131**, 1574
- Lada, E. A., & Lada, C. J. 1995, *AJ*, **109**, 1682
- Liu, M., et al. 2019, *ApJ*, **874**, 16
- López-Chico, T., & Salas, L. 2007, *RMxAA*, **43**, 155
- Lucas, P. W., et al. 2008, *MNRAS*, **391**, 136
- Maddox, N., et al. 2017, *MNRAS*, **470**, 2314
- Mateen, M., Hofner, P., & Araya, E. 2006, *ApJS*, **167**, 239
- McKee, C. F., & Ostriker, E. C. 2007, *ARA&A*, **45**, 565
- McKee, C. F., & Tan, J. C. 2003, *ApJ*, **585**, 850
- Megeath, S. T., et al. 1996, *A&A*, **307**, 775
- Megeath, S. T., et al. 2004, *ApJS*, **154**, 367
- Meyer, M. R., Calvet, N., & Hillenbrand, L. A. 1997, *AJ*, **114**, 288
- Miller, G. E., & Scalo, J. M. 1979, *ApJS*, **41**, 513
- Molinari, S., et al. 2016, *A&A*, **591**, A149
- Muzerolle, J., et al. 2004, *ApJS*, **154**, 379
- Neugebauer, G., et al. 1984, *ApJ*, **278**, L1
- Paron, S., Cichowolski, S., & Ortega, M. E. 2009, *A&A*, **506**, 789
- Persi, P., & Tapia, M. 2019, *MNRAS*, **485**, 784
- Peters, T., et al. 2010, *ApJ*, **711**, 1017
- Pezzuto, S., et al. 2021, *A&A*, **645**, A55
- Pilbratt, G. L., et al. 2010, *A&A*, **518**, L1
- Poglitsch, A., et al. 2010, *A&A*, **518**, L2
- Price, S. D., Egan, M. P., Carey, S. J., Mizuno, D. R., & Kuchar, T. A. 2001, *AJ*, **121**, 2819
- Qiu, K., et al. 2008, *ApJ*, **685**, 1005
- Rieke, G. H., & Lebofsky, M. J. 1985, *ApJ*, **288**, 618
- Rivera-Ingraham, A., et al. 2010, *ApJ*, **723**, 915
- Robitaille, T. P., Whitney, B. A., Indebetouw, R., & Wood, K. 2007, *ApJS*, **169**, 328
- Robitaille, T. P., Whitney, B. A., Indebetouw, R., Wood, K., & Denzmore, P. 2006, *ApJS*, **167**, 256
- Robitaille, T. P., et al. 2008, *AJ*, **136**, 2413
- Roy, A., et al. 2014, *A&A*, **562**, A138
- Salpeter, E. E. 1955, *ApJ*, **121**, 161
- Sánchez-Portal, M., et al. 2014, *ExA*, **37**, 453
- Scalo, J. M. 1986, *FCPh*, **11**, 1
- Schlegel, D. J., Finkbeiner, D. P., & Davis, M. 1998, *ApJ*, **500**, 525
- Siess, L., Dufour, E., & Forestini, M. 2000, *A&A*, **358**, 593
- Simon, R., Jackson, J. M., Clemens, D. P., Bania, T. M., & Heyer, M. H. 2001, *ApJ*, **551**, 747
- Solin, O., Ukkonen, E., & Haikala, L. 2012, *A&A*, **542**, A3
- Stern, D., et al. 2005, *ApJ*, **631**, 163
- Vig, S., Ghosh, S. K., Kulkarni, V. K., Ojha, D. K., & Verma, R. P. 2006, *ApJ*, **637**, 400
- Williams, J. P., & McKee, C. F. 1997, *ApJ*, **476**, 166
- Wood, D. O. S., & Churchwell, E. 1989, *ApJS*, **69**, 831
- Wright, E. L., et al. 2010, *AJ*, **140**, 1868
- Wu, Y. W., et al. 2019, *ApJ*, **874**, 94
- Zinnecker, H., McCaughrean, M. J., & Wilking, B. A. 1993, in *Protostars and Planets III*, ed. E. H. Levy, & J. I. Lunine, **429**
- Zinnecker, H., & Yorke, H. W. 2007, *ARA&A*, **45**, 481